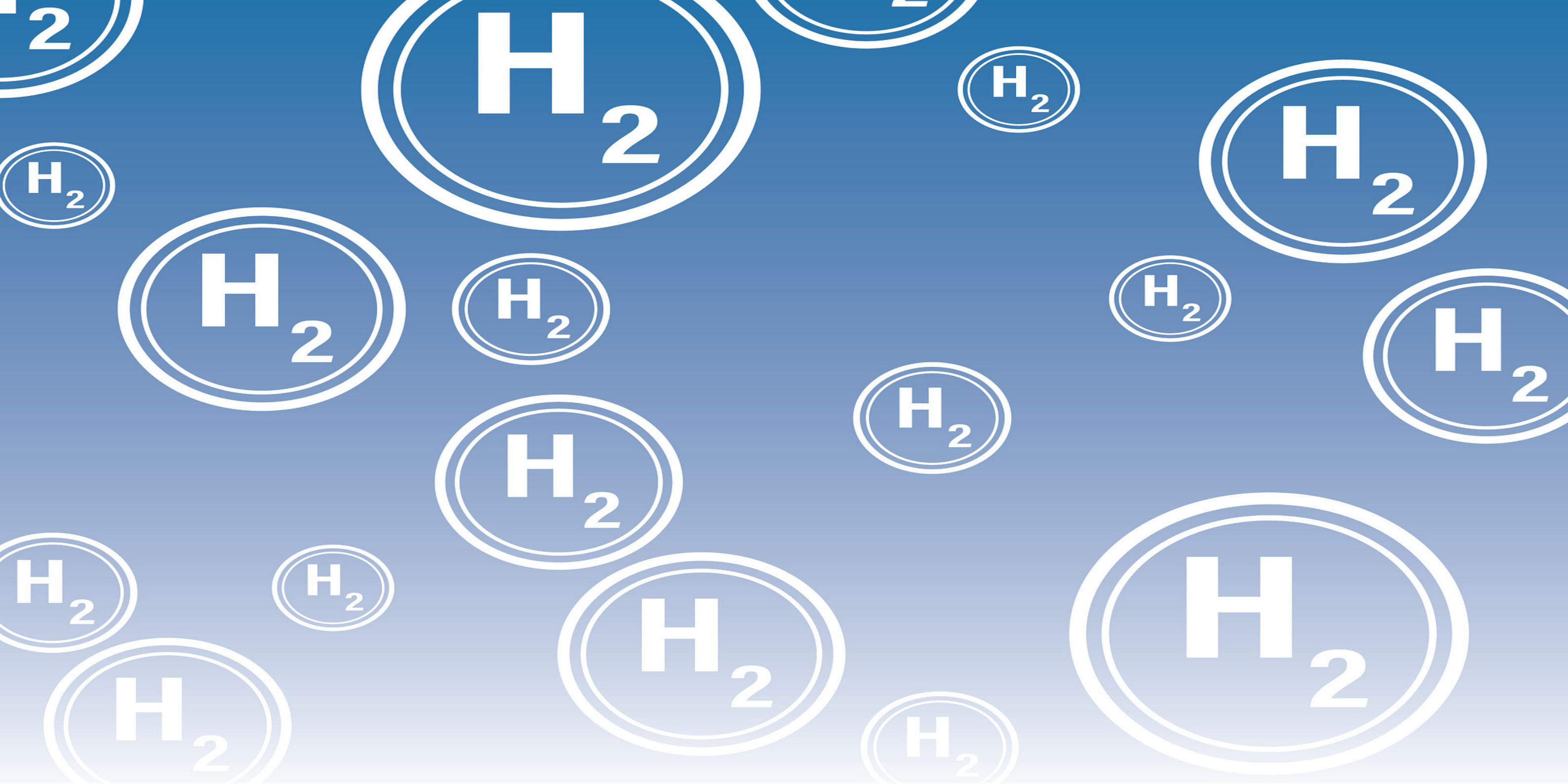

Electrochemical Based Modeling of Alkaline Water Electrolysis

Magnus Sejr Adamsen

Energy Technology, TEPE4-1006, 2022-06

Master's Project

STUDENT REPORT
AALBORG UNIVERSITY

Electrochemical Based Modeling of Alkaline Water Electrolysis

Magnus Sejr Adamsen

Energy Technology, TEPE4-1006, 30.05.2022

STUDENT REPORT

AALBORG UNIVERSITY

Energy Technology
Aalborg University
http://www.aau.dk

AALBORG UNIVERSITY
STUDENT REPORT

Title:
Electrolysis

Theme:
Alkaline water electrolysis

Project Period:
Spring Semester 2022

Project Group:
TEPE4-1006

Participant(s):
Magnus Sejr Adamsen

Supervisor(s):
Samuel Simon Araya
Vincenzo Liso

Copies: 1

Page Numbers: 63

Date of Completion:
May 30, 2022

Abstract:

Klimakrisen er en af nutidens største udfordringer, skyldtes vores afhængige af fossile brændstoffer. Der er stor enighed om at variable vedvarende energikilder, som vind og sol in sammenarbejde med energi lagring i stor skala er løsningen. Grønt hydrogen, produceret gennem elektrolyse er set som en meget lovende energi lagring teknologi. Modellering af vand elektrolyse celler er derfor afgørende for hvordan fremtidens energi lagring infrastruktur kommer til at se ud. I denne rapport fremlægges metoder til at bygge en model der forudsiger den statiske og dynamiske ydeevnen af et alkalisk vandelektrolyseanlæg baseret på elektrokemisk teori. Modellen er tilpasset målte data fra et industrielt vandelektrolyseanlæg og kan forudsige den statiske ydeevne med en forklaringsgrad over $r^2 > 98\%$. Det blev vist ved brug af overskydende energiproduktion fra vind og sol at en energi effektivitet på omkring $\varepsilon_{cell} \approx 75\%$ kunne opnås. Ydermere blev det vist at energi effektiviteten af den modellerede vandelektrolyseanlæg anvendt til frekvens regneregler var ligeledes høj omkring $\varepsilon_{cell} \approx 73\%$.

Nomenclature

Symbols		Units
α	Effective transfer coefficient	-
β	Symmetry factor	-
ΔG	Change in Gibbs free energy	kJ $\cdot mol^{-}1$
ΔH	Change in Enthalpy	kJ $\cdot mol^{-}1$
$\Delta N_{H_2,loss}$	Hydrogen leakage	mol
ΔQ_{irrev}	Irreversible heat	J
ΔQ_{rev}	Reversible heat	J
ΔS	Change in Entropy	kJ $\cdot mol^{-}1 \cdot K^{-}$
$\dot{m}$	mass flow	kg $\cdot s^{-1}$
ϵ	Effectiveness coefficient	-
ν	Stoichiometric coefficient	-
ρ	Mass density	kg $\cdot m^{-3}$
ε_{cell}	Energy efficiency coefficient	%
$\varepsilon_{faradiac}$	Energy efficiency coefficient	%
A	Surface area	m^2
$a\{H_2\}$	Thermodynamic activity of hydrogen	-
$a\{H_2O\}$	Thermodynamic activity of water	-

$a\{O_2\}$	Thermodynamic activity of oxygen	-
C_P	Specific Heat capacity	J $\cdot kg^{-1} \cdot K^{-1}$
C_r	Ration of C_min to C_max	-
C_{KOH}	molarity of potassium hydroxide	mol $\cdot L^{-1}$
C_{max}	Highest heat capacity of streams in heat exchanger	W $\cdot K^{-1}$
C_{min}	Lowest heat capacity of streams in heat exchanger	W $\cdot K^{-1}$
C_{tot}	Total heat capacity of the system	J $\cdot K^{-1}$
D	Diameter	m
e	Emissivity	-
E_a	Activation energy	J
E_c	Number of cell in the AWE stack	-
F	Faraday's constant	C $\cdot mol^{-1}$
h	Heat transfer coefficient	W $\cdot m^{-2} \cdot K^{-1}$
I	Current	A
i	Current density	A $\cdot cm^{-1}$
i_0	Exchange current density	A $\cdot cm^{-1}$
k	Area-specific conductivity	m $\cdot$
L	Length	m
M	Molar mass	kg $\cdot mol^{-1}$
P_{sat}	Vapour pressure	Pa
$Power_{stack}$	Power consumed by the AWE stack	MW
q	Heat transferred	W
Q_{amb}	Heat lost to the surroundings	W
Q_{in}	Heat added to the system	W
Q_{liq}	Heat removed by the flow of electrolyte	W
Q_{loss}	Heat generated by the water-splitting process	W

q_{max}	Maximum possible heat transferred	W
Q_{out}	Heat flowing out of the system	W
R	Universal gas constant	J $\cdot K^1 \cdot mol^1$
r	Least square residual	-
R_{an}	Anode resistance	
R_{cat}	Cathode resistance	
R_{ele}	Electrolyte resistance	
R_{mem}	Membrane resistance	
SS_{res}	Sum of squared residuals	V
SS_{tot}	Total sum of squared residuals	V
T	Temperature	K
t	Time	s
U_{act}	Activation over potential	V
U_{ohm}	Ohmic over potential	V
U_{rev}	Reversible potential	V
U_{tn}	Thermal neutral potential	V
W_{irrev}	Energy requirement under irreversibleconditions	J
W_{rev}	Energy requirement under reversible conditions	J
$wt\%$	Mass concentration	%

Subscripts

act	Activation
an	Anode
c	Cold
cat	Cathode
$cell$	Cell

ele	Electrolyte
f	Formation
h	Hot
i	Component superskcript
i	In
irrev	Irreversible
max	Maximum
mem	Membrane
min	Minimum
o	Out
ohm	Ohmic
pdt	Products
R	Reaction
rct	Reactants
res	Residual
rev	Reversible
sat	Saturation
stack	The stack AWE cells
th	Thermal neutral
tot	Total

Abbreviations

AWE	Alkaline water electrolysis	-
HER	hydrogen evolution reaction	-
IRES	Intermittent renewable energy sources	-
NTU	Number of Transfer Units	-
OER	oxygen evolution reaction	-

OR	Overall reaction	-
PEM	Polymer electrolyte membrane	-
PtX	Power to x	-
RDS	Rate-Determining Step	-
$SOEC$	solid oxide electrolysis cell	-
WE	Water electrolysis	-

Superscripts

0	At standard conditions superscript
i	Component superscript

Chemical formulas

CO_2	Carbon dioxide
e^-	Electron
H_2	Hydrogen
H_2O	Water
KOH	Potassium hydroxide
N_2	Nitrogen
$NaOH$	Sodium hydroxide
NH_3	Ammonia
O_2	Oxygen
OH^-	Hydroxide

Contents

Nomenclature vii

Preface xvii

1 Introduction 1

2 Scope of The Project 5
- 2.1 **Problem statement** 7

3 Electrochemical Performance Model 9
- 3.1 Reversible Potential 9
  - 3.1.1 Thermodynamics 9
- 3.2 Activation Over Potential 13
- 3.3 Ohmic Over Potential 15
  - 3.3.1 Electrolyte resistance: R_{ele} 15
  - 3.3.2 Membrane resistance: R_{mem} 17
  - 3.3.3 Electrode resistance: R_{cat} & R_{an} 17
- 3.4 Efficiency of the system 17
- 3.5 Data fitting the polarization curve 19

4 Heat Balance 23
- 4.1 Heat generated: Q_{loss} 24
- 4.2 Heat lost to the surroundings: Q_{amb} 25
- 4.3 Heat removed by the flow of electrolyte: Q_{liq} 25
- 4.4 Heat exchanger 26
- 4.5 P Controller 28

5 System dynamics 29
- 5.1 Dynamic response to current step 29
- 5.2 Dynamic heating process 33
- 5.3 Dynamic cool down process 38

6 System dynamics using Intermittent Renewable Energy Sources 41
6.1 Surplus from intermittent renewable energy sources 41
6.2 Dynamic respond to excess wind power 44
6.3 Dynamic respond to excess solar power 47

7 Dynamic Grid Frequency Regulation 51

8 Discussion 57

9 Conclusion 59

Bibliography 61

Summary

Decarbonisation is a big focus in reason years and intermittent renewable energy sources like wind and solar are predicted to be replacing the old fossil-fueled energy infrastructure. Switching to intermittent renewable energy sources will create the need for large scale energy storage. Here hydrogen production with electrolysis is seen as a promising solution as hydrogen is an excellent energy carrier with many uses that can help with the conversion away from fossil-fueled energy infrastructure.

In this report, a description of the methods used to model the static and dynamic performance of the alkaline water electrolysis process will be given. Starting with the static performance model electrochemically based modelling is used to predict the cell potential based on current density, electrolyte composition, pressure and temperature. The performance model is fitted to data from a real alkaline water electrolysis system and was able to predict the performance with an r-squared value over $r^2 > 98\%$. To model the dynamic behaviour of the alkaline water electrolysis process a zero-dimensional heat balance is set up to predict the change in temperature under load. Temperature control is implemented with a simple proportional feedback controller to ensure the system does not overheat.

To assess the performance, the model is subjected to different types of loads. The model is first tested under synthetic load to clearly illustrated how it behaves. The model is then subjected to excess power production from wind and solar showing how the performance is affected by the fluctuation of intermittent renewable energy sources. lastly, the concept of dynamic frequency regulation is introduced showing how hydrogen production through electrolysis can be used to help stabilise the grid frequency and how the model behaves in that mode of operation.

Preface

The following report has been developed by a student on the 4rd semester of Thermal Energy and Process Engineering at Aalborg University, under the theme: *Alkaline water electrolysis.* The citation in this report is done by showing [Author Year] in the text. The bibliography is written in the form:

[Author(s)],[Year],[Title],[URL]

All chapters and sections are provided with numbers presented in the table of contents. Figures, tables and equations have increasing numbers within each chapter.

Aalborg University, May 30, 2022

Magnus Sejr Adamsen

Magnus Sejr Adamsen
<msad@student.aau.dk>

Chapter 1

Introduction

On the 14th of July 2021, the European Commission presented the "Fit for 55" package which set the goal of a 55% net reduction of greenhouse gas emissions by 2030, as compared to 1990 levels [European Union 2021].

One way of reducing the CO_2 emissions is to reduce the consumption of fossil fuels and replace the energy production with renewable energy sources like wind, geothermal, solar and hydropower. Of these, wind and solar are classified as intermittent renewable energy sources (IRES). The issue with IRES is the fluctuating nature of them. This means that energy production from IRES does not follow the demand for energy. Other than not having energy when it is needed a surplus or deficit of energy can also affect the grid frequency.

Large scale energy storage will be a necessity to even out the fluctuating power of IRES. Currently, there are many different energy storage technologies available for example hydro pumping, thermal energy storage and battery storage. Each of the technologies has advantages and disadvantages. Hydro pumping is limited to geographical locations with large water reserves and height differences whereas thermal energy storage and battery storage are not. Battery storage is limited to smaller capacities due to the high cost.

In the plan presented by the danish government [government 2021] to reduce the net greenhouse gas emissions by 55%, power to x (PtX) is mentioned as one of the technologies that should be used to reach the goal by 2030. PtX is generally the process of converting electric energy to any other form of energy. PtX is however often used to describe the conversion of electrical power to chemical storing compounds. Hydrogen production with electrolysis is a promising PtX technology for many reasons. Electrolysis of water is a well know and developed technology first observed in 1789 and first used on a commercialized scale in the early 20th century for welding. In 1947 a 380 MW scale water electrolysis was constructed in Norway to produce ammonia using the Haber-Bosch-process seen below. [Godula-Jopek 2015]

$$N_2 + 3H_2 \rightarrow 2NH_3 \tag{1.1}$$

Hydrogen has many uses as a resource. It is the fuel used in fuel cells which might be a viable option to electrify heavy dude transportation such as trucks where the energy to the mass density of batteries is too low. Hydrogen is also be used together with CO_2 to produce methanol and in the proceed capture CO_2 from processes that can not be emissions neutral, for example cement production. Currently, most hydrogen production is grey hydrogen produces via steam reforming of fossil fuels. Here 48% is from Naturalgas, 30% from oil, 18% from coal and only 4% is green hydrogen from water electrolysis (WE). [Godula-Jopek 2015] Using WE to produce green hydrogen using excess energy from IRES would not only make it more feasible to implement IRES into the power grid but could also reduce the production of grey hydrogen which is currently responsible for 3% of the global CO_2 emissions [Soltani, Rosen, and Dincer 2014]. Currently, Three groups of technologies for WE exist. Solid oxide electrolysis SOEC, polymer electrolyte membrane electrolysis PEM and alkaline Water electrolysis AWE. SOEC is the newest and most efficient technology achieved via the high temperatures the cell operates at. SOEC has however not been shown to be a commercially viable due to high material cost and high degradation. The PEM technology has the advantage of being able to operate at high current densities at a high efficiency making the cells and stack smaller in size and is shown to be commercially viable. PEM cells are however using expensive and rare platinum group metal as a catalyst making them prohibitively expensive. Implementing the PEM technology as PtX for the IRES of the future might not be possible. It might be limited by the mining rate of the rare platinum group and would need a reduction of the amount of catalyst needed in PEM and a highly efficient recycling process [Minke et al. 2021]. AWE is the most mature of the technologies and the most commercially viable using cheap and abundant electrode material. AWE does, however, operate at lower current densities than both SOEC and PEM, making the AWE units much larger in size.

An AWE cell have four components. In Figure 1.1 a diagram of a AWE cell is showing each of the components. Two electrodes are submerged into an electrolyte and a potential difference is applied splitting the water in the electrolyte into hydrogen and oxygen. Hydrogen is created on the negative electrode called the cathode and oxygen on the positive anode. To improve the efficiency of the cell an alkaline compound is added which increases the ionic conductivity. The most common of these are sodium hydroxide (NaOH) and potassium hydroxide (KOH). Keeping the product gasses of the reaction separate is strictly necessary as the mixture of hydrogen and oxygen is a highly flammable gas. A separation membrane is then placed in between the two electrodes to keep the hydrogen and oxygen separated while still allow the transfer of ions.

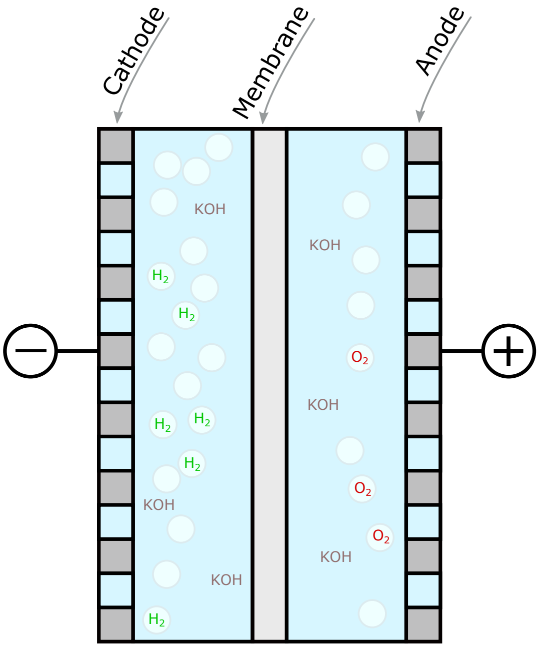

Figure 1.1: Diagram of components in an AWE cell.

The overall reaction for WE is shown in Table 1.1, where a water molecule is split into a hydrogen molecule and half an oxygen molecule per reaction. The reaction of the WE can also be described as a mechanism of reactions. One for the reaction at the negative electrode or cathode and one at the positive anode. These are the intermediate reactions referred to as the hydrogen evolution reaction (HER) and the oxygen evolution reaction (OER), respectively for the cathode and anode. The OER and HER are shown for AWE in Table 1.1. Each of the intermediate reactions is described by a mechanism.

Table 1.1: AWE

Electrode	Reaction
Cathode (HER):	$2H_2O + 2e^- \rightleftharpoons H_2 + 2OH^-$
Anode (OER):	$2OH^- \rightleftharpoons \frac{1}{2}O_2 + H_2O + 2e^-$
Overall:	$H_2O(l) \rightleftharpoons H_2 + \frac{1}{2}O_2$

In Figure 1.2 the reaction mechanism of the OER of AWE is illustrated graphically to show that two different pathways are possible for the creation of oxygen. Depending on the operating conditions one or the other will then be favoured influencing the overall reaction kinetics.

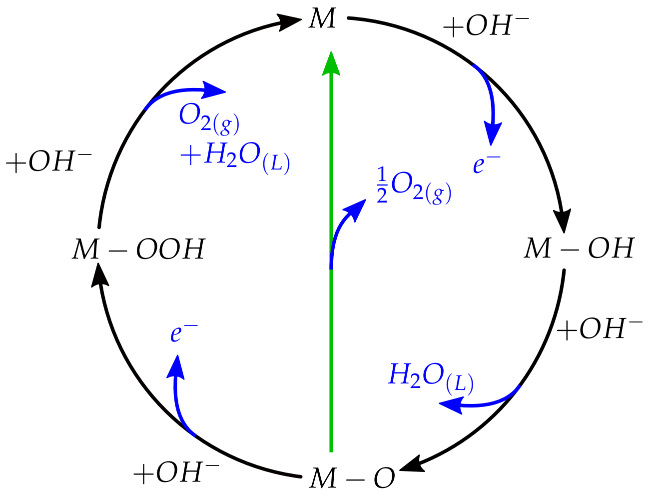

Figure 1.2: OER reaction mechanism for AWE. [Jiang 2020]

The Mechanism shown in the diagram in Figure 1.2 can also be represented as a series of chemical reactions where the sum of all steps must give the overall reaction (OR). In both the Figure 1.2 and the steps below M represents a catalytic site on the anode.

$$S_1: \quad OH^- + M \rightleftharpoons OH \cdot M + e^- \tag{1.2}$$

$$S_2: \quad OH \cdot M + OH^- \rightleftharpoons O \cdot M + H_2O + e^- \tag{1.3}$$

$$S_3: \quad O \cdot M + O \cdot M \rightleftharpoons O_2 \tag{1.4}$$

$$S_4: \quad O \cdot M + OH^- \rightleftharpoons OOH \cdot M + e^- \tag{1.5}$$

$$S_5: \quad OOH \cdot M + OH^- \rightleftharpoons O_2 + H_2O + e^- + M \tag{1.6}$$

$$OR: \quad 4OH^- \rightleftharpoons 2H_2O + O_2 + 4e^- \tag{1.7}$$

Chapter 2

Scope of The Project

In the article "Dynamic energy and mass balance model for an industrial alkaline water electrolyzer plant process" by [Sakas et al. 2022] a model of an AWE plant is proposed that predicts the steady performance and dynamic behaviour of an industrial-sized AWE plant through white-box modelling using zero-dimensional mass and energy balances. Data from an analogous industrial plant was obtained and the model was shown to predict the thermal dynamics with 98.7% accuracy.

The plant system diagram for the model by [Sakas et al. 2022] is shown in Figure 2.1. The system diagram includes a stack of AWE cells to produce hydrogen. The electrolyte is circulated to remove the gas from the AWE stack. Gas-liquid separators are used to separate hydrogen and oxygen from the electrolyte. Heat exchangers cool the electrolyte and are subsequently mixed in an agitation process before reentering the AWE stack again. The heat exchangers in the Diagram say "lye cooling" because the electrolyte is lye. Lye is the common term for aqueous solutions of KOH and or NaOH. A KOH aqueous solution is specifically used in this model. On the hydrogen side, deionized feed water is added to compensate for the removed gas and the hydrogen is separated from the electrolyte and into a purification process.

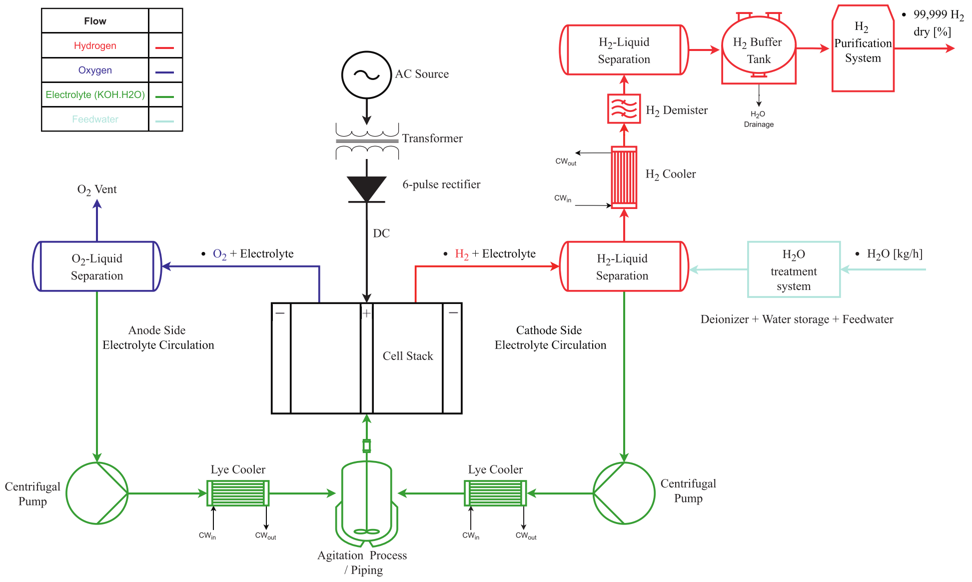

Figure 2.1: System diagram of the AWE plant as presented in [Sakas et al. 2022].

In this report the model will be based on the one from [Sakas et al. 2022] should be capable of predicting the steady performance and the dynamic behaviour of the AWE. The focus of the modelling will be to implement electronically theoretical based calculations where the model from [Sakas et al. 2022] is using empirically-based equations in hopes of creating a more general model.

The model developed in this report will be of a modified system diagram shown in Figure 2.2. Here the purification process and the AC/DC conversion are removed as the focus will be more on the performance of the AWE process. The two heat exchangers in Figure 2.1 will be replaced with a single heat exchanger after the mixing in the agitation process instead of before.

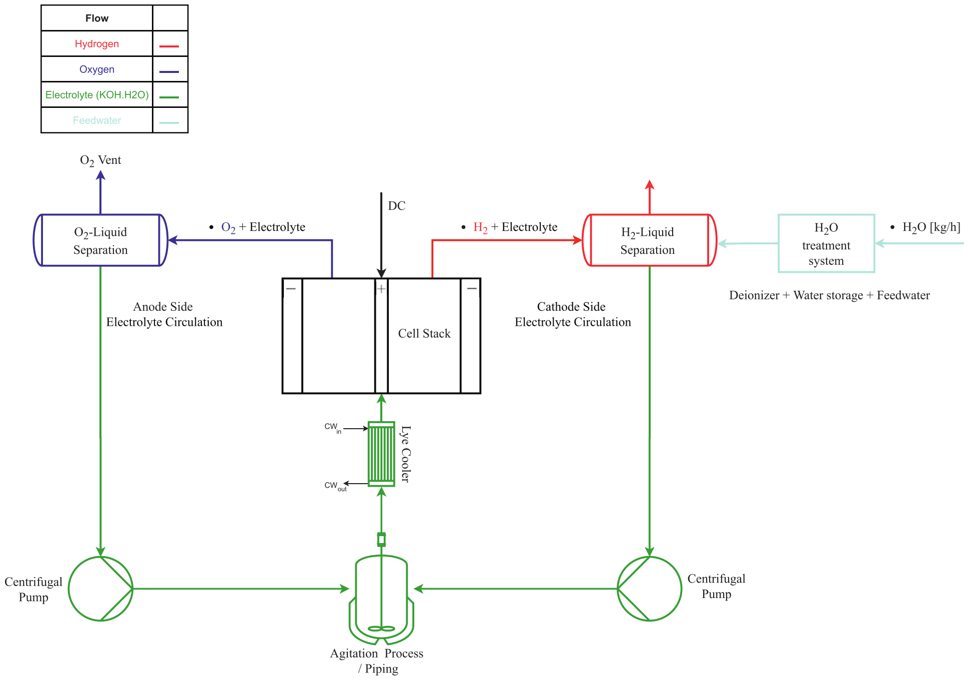

Figure 2.2: System diagram of the AWE plant modelled in this report. The figure is modified from the diagram from [Sakas et al. 2022].

Additionally, the model should be tested at different power inputs to see how the AWE process operates in different use cases. The performance of the system will be seen from the perspective of the AWE stack and only include the balance of plant (BOP) than directly influence the AWE stack.

2.1 Problem statement

Having explored the fundamentals of hydrogen production through water electrolysis and defined the scope of what the project sets out to model, the following problem statement has been formulated.

How can an AWE system be modeled to predict the static and dynamic performance given a DC power input and how does the system perform under different modes of operation?

Chapter 3

Electrochemical Performance Model

The polarization curve is a widely used metric to describe the performance of an electrochemical reactor which relates the cell potential with current density. As known from both theory and real measurement the cell potential of a real electrochemical cell is higher than the theoretical reversible potential. The real cell potential is therefore expressed as the reversible potential with additional over potentials as seen in Equation 3.1.

$$U_{cell} = U_{rev} + U_{act} + U_{ohm} \tag{3.1}$$

A description of each potential is given in the following sections along with the methods used to calculate them.

3.1 Reversible Potential

3.1.1 Thermodynamics

For the decomposition reaction involve with WE energy is required to break the bonds in water between hydrogen and oxygen. The energy associated is the reaction enthalpy ΔH_R and is calculated as the difference in the sum of enthalpies of formation between reactants and products as seen in Equation 3.2.

$$\Delta H_R = \sum \nu_{pdt} \Delta H_{f,pdt} - \sum \nu_{rct} \Delta H_{f,rct} \tag{3.2}$$

Here ν_{pdt} and ν_{rct} are the stoichiometric coefficients for the products and reactants respectively. $\Delta H_{f,pdt}$ $\Delta H_{f,rct}$ are the enthalpies of formation respectively for the products and reactants. By definition, the enthalpies of formation for hydrogen and oxygen are zero as is shown in Table 3.1. This has an interesting result for water electrolysis that the formation enthalpy of reaction is solely driven by waters enthalpy of formation. The water spitting reaction is driven by two forms of energy being electrochemical and thermal this is shown in Equation 3.3 by expanding the formation enthalpy of reaction into the formation of Gibbs free energy and entropy.

$$\Delta H_R = \Delta G_R + T \cdot \Delta S_R \tag{3.3}$$

The change in entropy for the reaction ΔS_R is defined similarly to the formation enthalpy of reaction in Equation3.4.

$$\Delta S_R = \sum \nu_{pdt} \Delta S_{f,pdt} - \sum \nu_{rct} \Delta S_{f,rct} \tag{3.4}$$

The product between temperature and the formation entropy of reaction represents the thermal energy needed for the reaction. The electrochemical energy is then associated with the formation of Gibbs free energy of reaction and is derived in Equation 3.5 from Equations 3.2, 3.3 and 3.4.

$$\Delta G_R = \sum \nu_{pdt} \Delta H_{f,pdt} - \sum \nu_{rct} \Delta H_{f,rct} - T \cdot \left[\sum \nu_{pdt} \Delta S_{f,pdt} - \sum \nu_{rct} \Delta S_{f,rct}\right] \tag{3.5}$$

A few interesting things can be said about the Gibbs free energy. It is the most used thermodynamic potential in chemistry and is defined as the theoretical maximum amount of thermodynamic work that can be extracted from a system where no volume work is done. The sign of the Gibbs free energy can tell if the reaction is spontaneous or if it needs additional energy to react. [Schroeder 2000 - 2000]

Under standard conditions, we can calculate the Gibbs free energy from the standard enthalpies and entropies of formation found in Table 3.1.

The enthalpies and entropies of formation are however temperature dependent and the electrical energy that is needed for the water-splitting reaction is therefore changing with temperature as shown in Figure 3.1. Here it is shown that for higher temperatures less energy needs to be supplied electrical to slit water which is the reason why water electrolysis cells are operated at elevated temperatures. The sudden change at $373.2K$ is the phase change going from liquid water to steam. Electrolysis cells using liquid water like AWE and PEM are however limited to operate under the boiling point. A water electrolysis technology that is not limited by the boiling point is the SOEC which operated at temperatures between 500 and $900°C$ ["Peter Styring" 2015] making it highly efficient. Following the evolution of the graph to the extreme of $3000°C$ Gibbs free energy changes sign and the reaction of water, splitting becomes spontaneous.

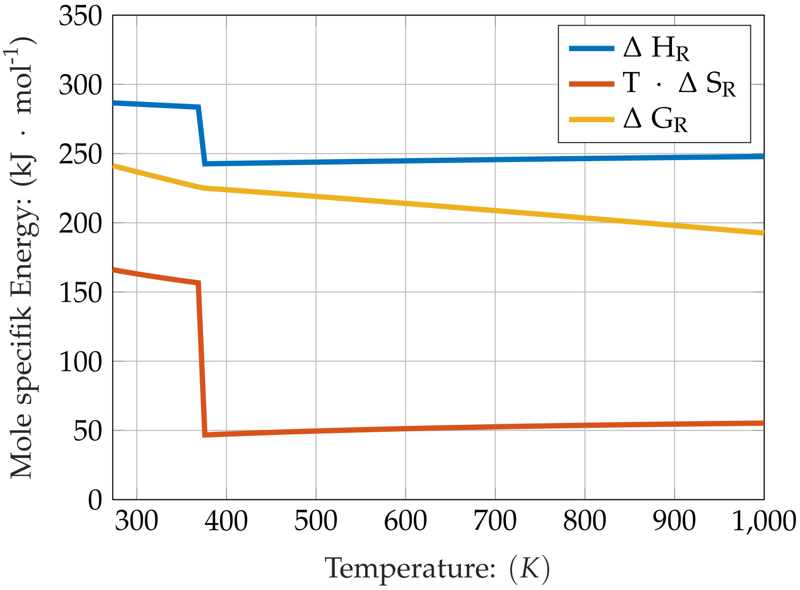

Figure 3.1: Formation Enthalpy and entropy, calculated using numerical formulas and methods from [*NASA Glenn Coefficients for CalculatingThermodynamic Properties ofIndividual Species* 2002].

Table 3.1: enthalpies of formation. [Spiegel 2008]

Substance (State of Matter)	$\Delta H_R^0(kJmol^-1)$	$\Delta S_R^0(kJmol^-1K^-1)$
H_2O (l):	-285.83	69.942
H_2 (g):	0	131.337
O_2 (g):	0	205.817

Using Equation 3.6 the energy needed for the reaction, the Gibbs free energy can be associated with electrical potential. Her F is Faraday's constant which represents the electric charge carried by one mole of electrons and z is the number of electrons transferred per reaction. Under standard conditions the potential is show in Equation 3.6 to be $1.229V$.

$$U_{rev}^0 = \frac{\Delta G_{ref}^0}{z \cdot F} = 1.229V \tag{3.6}$$

The Gibbs free energy is not simply a function of temperature but also pressure therefore to calculate the reversible potential at operating conditions Nernst equation can be used seen in Equation 3.7. Her R is the universal gas constant and a is the activities of the different components.

$$U_{rev} = U_{rev}^{0} - \frac{R \cdot T}{2 \cdot F} \cdot ln\left(\frac{a\{H_2O\}}{a\{H_2\} \cdot a\{O_2\}^{1/2}}\right) \tag{3.7}$$

It is through thermodynamic activities the pressure affect Gibbs free energy. Thermodynamic activity is the property defined as the ratio between the fugacity of the pure component to the fugacity of the solution. Fugacity is defined as the product between the fugacity coefficient and the real gas pressure. For an ideal gas, the fugacity is equal to the gas pressure and the fugacity coefficient is unity. Vapour pressures are usually relatively low and the gas can be assumed to behave ideal and activity can be estimated as the partial pressure of the components. [Gaskell 2001]

Assuming that the partial pressure of both hydrogen in the cathode chamber and oxygen in the anode chamber is equal to the vapour pressure of water the Antoine equation can use to calculate the partial pressure of the products.

$$\begin{aligned} P_{sat,H_2O} &= 10^{A-B/(C+T)} \\ A &= 5.1962 \\ B &= 1730.63 \\ C &= 233.426 \end{aligned}$$

Because the electrolyte of used in AWE is not purely water but an aqueous solution of KOH the vapour pressure is slightly different. In [Sakas et al. 2022] an empirical equation is used to calculate the vapour pressure of the electrolyte shown below in Equation 3.8. Here a and b are numerically determined polynomial as a function of molarity of KOH seen in Equation 3.9.

$$P_{sat,KOH} = \exp(2.302 \cdot a + b \cdot ln(P_{sat,H_2O})) \tag{3.8}$$

$$a = -0.0151 \cdot C_{KOH} - 1.6788 \cdot 10^{-3} \cdot C_{KOH}^{2} + 2.2588 \cdot 10^{-5} \cdot C_{KOH}^{3} \tag{3.9}$$

$$b = 1 - 1.2062 \cdot 10^{-3} \cdot C_{KOH} + 5.6024 \cdot 10^{-4} \cdot C_{KOH}^{2} - 7.8228 \cdot 10^{-6} \cdot C_{KOH}^{3} \tag{3.10}$$

The activity of the product gasses are then calculated using the partial pressures and the total pressure as shown inn Equation 3.11 and 3.12.

$$a\{H_2\} = \frac{(P_{tot} - Psat, KOH)}{P_{tot}} \tag{3.11}$$

$$a\{O_2\} = \frac{(P_{tot} - Psat, KOH)}{P_{tot}} \tag{3.12}$$

To calculated the activity for water $a\{H_2O\}$ another empirical based expression is used from [Sakas et al. 2022] shown in Equation 3.13.

$$a\{H_2O\} = exp(-0.05192 \cdot C_{KOH} + 0.003302 \cdot C_{KOH}^2 + \frac{3.177 \cdot C_{KOH} - 2.131 \cdot C_{KOH}^3}{T}) \tag{3.13}$$

having now describe the method of calculating the reversible potential the following sections will focus on the over potentials with can be seen as various losses of the cell.

3.2 Activation Over Potential

In addition to the energy of formation, needed to split water into hydrogen and oxygen, activation energy is needed for the reaction to take place. Activation energy is often described by the analogy of rolling a rock down a hill with a smaller mound on top that need to be overcomed as illustrated in Figure 3.2. The illustration shows that even if the rock would roll to the lower part of the hill it can not do so without being pushed over the mound first. The same is true for some chemical reactions as it might be energetically favourable for a reaction to occur it needs a little extra energy to react. This is also the reason why things like books does not just spontaneously burst into flames even though it is energetically favourable.

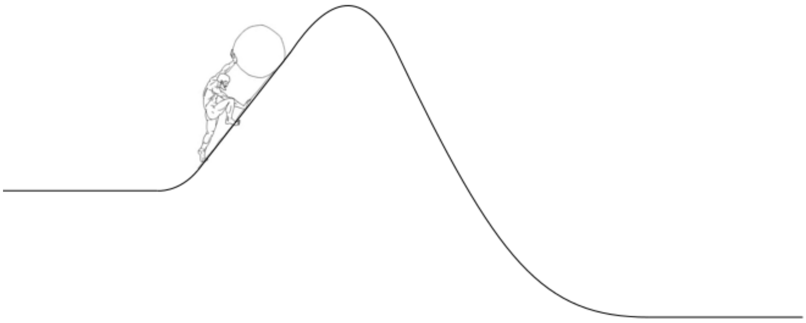

Figure 3.2: Illustration on the concept of activation energy.

For the water electrolysis, we are concerned with the over potentials U_{act} associated with the activation energy. Assuming the reaction mechanism for water splitting is limited by a single rate-determining step RDS we can use i single butler-Volmer equation seen bellow in Equation 3.14. Her i is the current density, i_0 is the exchange current density β is the symmetry factor, F is Faradays constant, ν_{e^-} is the stoichiometric coefficient of electrons, U_{act} is the activation over potentials, R is the universal constant and T is the Temperature.

$$i = i_0 \left[\exp\left\{ \frac{(\beta)\, \nu_{e^-}\, F\, U_{act}}{RT} \right\} - \exp\left\{ \frac{(\beta - 1)\, \nu_{e^-}\, F\, U_{act}}{RT} \right\} \right] \tag{3.14}$$

For simplification the symetricfactor can be assumed $\beta = 1/2$ which is a fair assumption for elementary reaktions [Jiang 2020]. With this assumption the Butler-Volmer can be reformulated into Equation 3.15. Then isolating for the U_{act} an expression of the activation over potential is given in Equation 3.16.

$$i = i_0 \left\{ 2\, \sinh\left(\frac{\beta\, \nu_{e^-}\, F\, U_{act}}{RT} \right) \right\} \tag{3.15}$$

$$U_{act} = \left(\frac{RT}{\beta\, \nu_{e^-}\, F} \right) \sinh^{-1}\left(\frac{i}{2 i_0} \right) \tag{3.16}$$

To calculate the activation over potential U_{act} as a function of current density and temperature from Equation 3.16 ν_{e^-} and i_0 are still to be determined. These parameters differ from the HER at the cathode to the OER at the anode. The exchange current density can be seen as the rate of reaction and it is in fact connected to it shown in Equation 3.17.

$$i_0 = F\, \nu_{e^-}\, k \tag{3.17}$$

The rate of reaction is defined by Arrhenius equation 3.18 and is in this way related to temperature and activation energy. In this report, the exchange current densities will be used as fitting parameters to fit the polarization curve to data from a industrial sized AWE plant obtained from [Sakas et al. 2022]. A detail description of the method used for fitting the exchanger current densities will be given at the end of the chapter in Section 3.5.

$$k = A e^{E_a/RT} \tag{3.18}$$

The stoichiometric coefficient of electrons ν_{e^-} is dependent on what the RDS is of the reaction mechanism shown in Figure 3.3 which can change depending on the operating conditions. [Demitri et al. 2016]

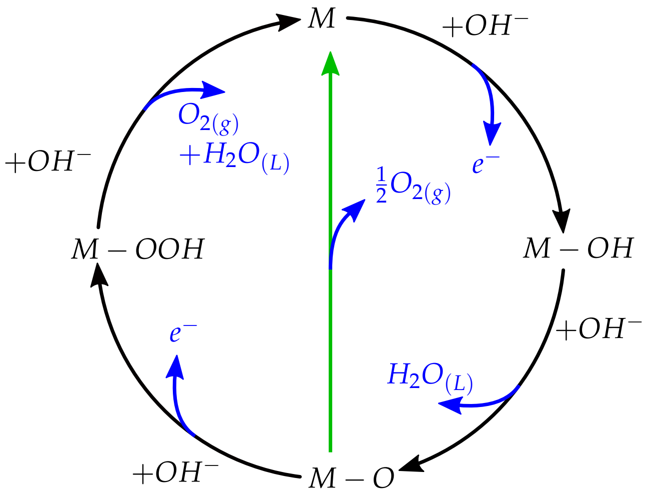

Figure 3.3: OER reaction mechanism for AWE. [Jiang 2020]

Often however the stoichiometric coefficient of electrons ν_{e^-} and the symetricfactor β are combined and the product is refereed to as the effective transfer coefficient α. The effective transfer α_{cat} and α_{an} coefficients of the anodic reaction (OER) and cathodic reaction (HER) respectively are normally assumed to be 0.5 [Jiang 2020] and will also be done in this report.

3.3 Ohmic Over Potential

The last over potential included in this model is the over potential coming from ohmic resistance in the electrolysis cell. The resistance can be split into four different parts associated with a different parts of the cell components. There are two resistances from the electrodes the R_{an} for the anode and R_{cat} for the cathode. The gas impervious membrane does also create resistance R_{mem} and lastly the electrolyte has resistance R_{ele}.
The over potential created from these residences are calculated as seen in Equation 3.19

$$U_{ohm} = i \cdot (R_{ele} + R_{mem} + R_{an} + R_{cat}) \tag{3.19}$$

3.3.1 Electrolyte resistance: R_{ele}

The resistance that the electrolyte creates is expressed in Equation 3.20 where k is the conductivity and L_{ele} is the length between the electrodes occupied by the electrolyte.

$$R_{ele} = \frac{1}{k} \cdot L_{ele} \tag{3.20}$$

It can be seen that the resistance is linearly proportional to the distance between the electrodes. Therefore this gap is made as small as possible to minimise resistance. It can also be seen that the resistance is inverse linear proportional to the conductivity. Therefore solvents are added to the electrolyte to increase its conductivity of the electrolyte. For the following model it will be assumed that the electrolyte is an aqueous solution of KOH and the conductivity is modelled using a polynomial expression derived from experimental data done by [Gilliam et al. 2007]. The polynomial is shown in Equation 3.21 and calculates the conductivity as a function of the morality of KOH in water and temperature. The values of A,B,C,D,E and F are constant that can be found in [Gilliam et al. 2007].

$$
\begin{aligned}
k =& A \cdot C_{KOH}^{1} && (3.21)\\
&+B \cdot C_{KOH}^{2} && (3.22)\\
&+C \cdot C_{KOH} \cdot T && (3.23)\\
&+D \cdot C_{KOH} \cdot T^{-1} && (3.24)\\
&+E \cdot C_{KOH}^{3} && (3.25)\\
&+F \cdot C_{KOH}^{2} \cdot T^{2} && (3.26)
\end{aligned}
$$

Usually, the concentration of KOH is not specified in morality but as a weight percentage. Therefore the model will include a conversion calculation shown in Equation 3.27. Here C_{KOH} is the morality of the aqueous solution of KOH, $wt\%$ is the concentration in weight percentage and ρ_{ele} is the density of the aqueous solutions.

$$C_{KOH} = wt\% \cdot \frac{\rho_{KOH}}{C_{KOH}} \tag{3.27}$$

For the density, an additional equation from [Gilliam et al. 2007] is used shown in Equation 3.28 here A, B and C are empirically measurement dependent on temperature and can be found in [Gilliam et al. 2007].

$$\rho_{KOH} = A \cdot C_{KOH}^{2} + B \cdot C_{KOH} + C \tag{3.28}$$

With equations 3.21 to 3.28 the conductivity is plotted in Figure 3.4 here it can be seen that conductivity increases with temperature and is highest at a concentration around $C_{KOH} = 8 mol/L$ corresponding to a $wt\% = 25\%$ mass fraction.

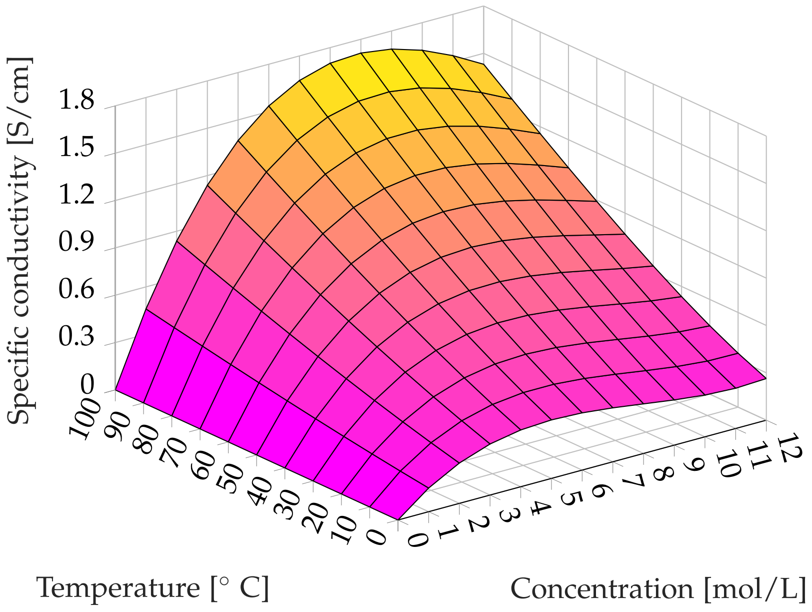

Figure 3.4: Conductivity of the electrolyte at different temperature and molarity of KOH

3.3.2 Membrane resistance: R_{mem}

In the alkaline electrolysis cell, a separating membrane is used to keep the gases separated which is a necessity for safety reasons as the mixture of hydrogen and oxygen is a highly volatile mixture that can explode at very low contamination levels. The membrane has an ionic resistance which is given by the manufacturer of Zirfon at $0.2935[\Omega \cdot cm^2]$. The study [Rodríguez et al. 2019] uses a precise approach to determine the membrane resistance R_{mem} and found that the values from the manufacturer were in good agreement with their result. They also found that the resistance was pretty stable under different operating conditions and at different levels of ageing. Therefore the constant value of $0.2935[\Omega \cdot cm^2]$ will be used in this project.

3.3.3 Electrode resistance: R_{cat} & R_{an}

The resistance in the electrodes is electrical in nature and is orders of magnitude lower than the ionic resistance of the electrolyte and membrane. Therefore they are considered negligible and are not included in the model.

3.4 Efficiency of the system

Calculating the efficiency of the AWE plant is a key aspect of assessing the performance of the plant under operation. As is the case for many energy converting systems more than one formulation of efficiency can be made depending on what is of interest. The theoretical energy efficiency coefficient ε_{Cell} for the WE process is defined as the fraction between the energy requirement under reversible conditions to split water W_{rev} and the energy requirement under irreversible conditions W_{irrev} as shown in Equation 3.29. This efficiency is limited to a maximum of unity as the irreversible work W_{irrev} is equal to the reversible work W_{rev} only under equilibrium when the current is zero and larger in any other case when the current is non zero. [Lamy and Millet 2020]

$$\varepsilon_{Cell} = \frac{\text{energy requirement under reversible conditions}}{\text{energy requirement under irreversible conditions}} = \frac{W_{rev}}{W_{irrev}} \tag{3.29}$$

The reversible work is defined as the sum of the electrical work ΔG_{rev} and the reversible heat ΔQ_{rev} as shown in Equation 3.33. The irreversible work is defined as the sum of the reversible work and the irreversible heat ΔQ_{irrev} shown in Equation 3.30.

$$\begin{aligned} W_{rev} &= \Delta G_{rev} + \Delta Q_{rev} && (3.30)\\ &= nF\ U_{rev} + nF\ (U_{tn} - U_{rev}) && (3.31)\\ &= nF\ U_{tn} && (3.32) \end{aligned}$$

$$\begin{aligned} W_{irrev} &= \Delta G_{rev} + \Delta Q_{rev} + \Delta Q_{irrev} && (3.33)\\ &= nF\ U_{rev} + nF\ (U_{tn} - U_{rev}) + nF\ (U_{cell} - U_{rev}) && (3.34)\\ &= nF\ U_{tn} + nF\ (U_{cell} - U_{rev}) && (3.35) \end{aligned}$$

With the reversible work and irreversible formulated as functions of potentials the theoretical energy efficiency coefficient ε_{Cell} can be reformulated as shown in Equation 3.36.

$$\varepsilon_{Cell} = \frac{U_{tn}}{U_{tn} + U_{cell} - U_{rev}} \tag{3.36}$$

A mass conservation efficiency also exists for the WE process this is the faradaic efficiency. This is defined as the hydrogen produced over a time period over the theoretical hydrogen produced according to Faraday's law. The Faradaic efficiency can be formulated as shown in Equation 3.30.

$$\varepsilon_{Faradaic} = \frac{I\Delta t/2F - \Delta N_{H_2,loss}}{I\Delta t/2F} \tag{3.37}$$

The loss of hydrogen $\Delta N_{H_2,loss}$ can be caused by parasitic electrochemical reactions or leakage of hydrogen from the anode to the cathode chamber ether by leaking through the electrolyte separator membrane or by inefficient separation in the gas-liquid separators. In the model developed in [Sakas et al. 2022] a constant Faradaic efficiency coefficient of $\varepsilon_{Faradaic} = 0.86$ is used and will be in this report as well. The Faradaic efficiency will be used later on in the report chapter 4 to evaluate mass balances.

3.5 Data fitting the polarization curve

To insure that the model can predict the performance of a real system the model is fitted to measured data. The model will be fitted to data from [Sakas et al. 2022] where the polarization curve at three temperatures where measured. The data is shown in Figure 3.5 and was collected from an industrial sized AWE system operating under 16 bar of pressure at temperatures of $70°C, 61.5°C, 59.6°C$.

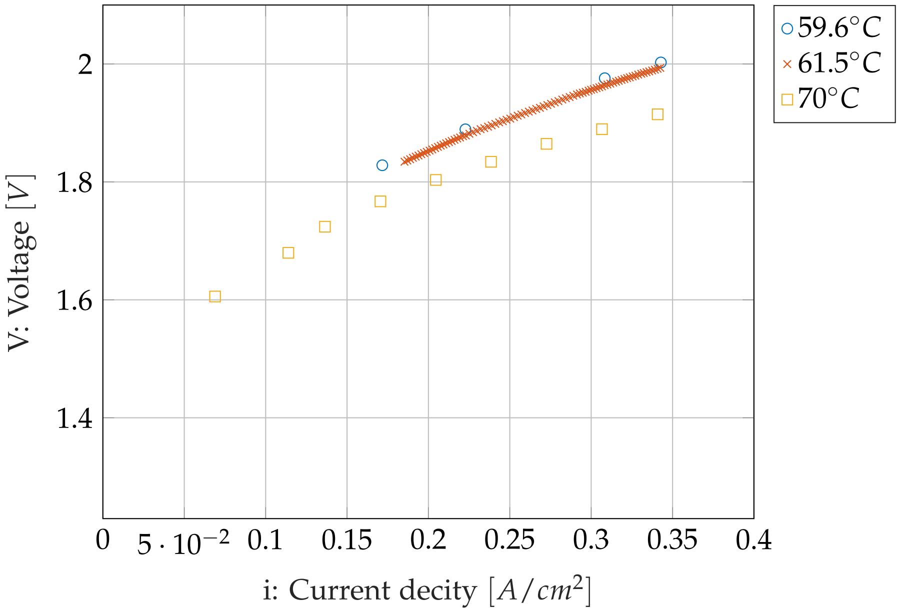

Figure 3.5: Measured polarization curve of an industrial sized AWE system at different temperatures. [Sakas et al. 2022]

To fit the model the exchange current densities used as fitting parameters. In [Sakas et al. 2022] it is specified that the electrodes are coated in a alloy of nickel and cobalt.

In [Lupi, Dell'Era, and Pasquali 2009] the exchange current densities for cathodes coated with nickel-cobalt alloys of different compositions have been found. As the composition nickel-cobalt alloy is not mentioned in [Sakas et al. 2022] the composition with the best fitting exchange current density was chosen as a reference. Due to the slower reaction rate of the OER the exchange current density for the anode $i_{0,an}$ is typically much lower than for the cathode. Therefore $i_{0,an}$ was simply estimated to be linearly related to the reference $i_{0,cat}$ by a factor. In [Demitri et al. 2016] an example sets $i_{0,an}$ roughly 9 order lower than $i_{0,cat}$ and a factor of $10^{-}9$ is therefor used between the exchange current densities in the model.

To quantify the fitness of the model to the data a least square residual is calculated as shown in Equation 3.38. Her SS_{res} is the sum of squared residuals, also called the residual sum of squares and is calculated as seen in 3.39. SS_{tot} is the total sum of squares calculated as seen in Equation 3.40.

$$r = \sqrt{1 - \frac{SS_{res}}{SS_{tot}}} \tag{3.38}$$

$$SS_{res} = \sum (U_{data} - U_{model})^2 \tag{3.39}$$

$$SS_{tot} = \sum (\overline{U_{data}} - U_{model})^2 \tag{3.40}$$

The reference exchange current density for cathodes $i_{0,cat}$ is then adjusted to give the best fit for each data set of the polarisation curve. In Figure 3.6 the exchange current densities were fitted to $i_{0,cat} = 1.5 \cdot 10^{-}5(A/cm2)$ and $i_{0,an} = 1.5 \cdot 10^{-}14(A/cm2)$ giving a squared residual over $r^2 = 99\%$ at a temperature of $59.6°C$.

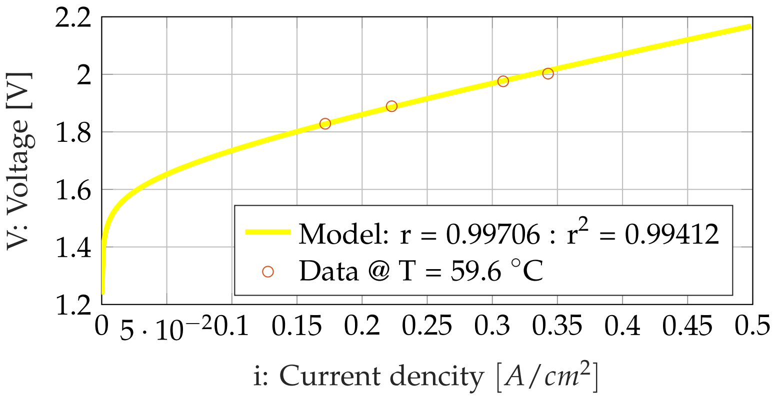

Figure 3.6: Model fitted to measured polarization curve at $T = 59.5°C$.

In Figure 3.7 the exchange current densities were fitted to $i_{0,cat} = 1.7 \cdot 10^{-}5(A/cm2)$ and $i_{0,an} = 1.7 \cdot 10^{-}14(A/cm2)$ giving a squared residual over $r^2 = 99\%$ at a temperature of $61.5°C$.

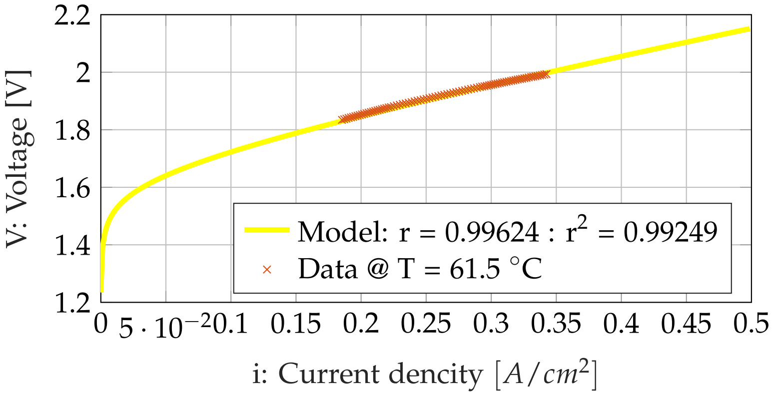

Figure 3.7: Model fitted to measured polarization curve at $T = 61.5°C$.

In Figure 3.8 the exchange current densities were fitted to $i_{0,cat} = 5.3 \cdot 10^{-}5(A/cm2)$ and $i_{0,an} = 5.3 \cdot 10^{-}14(A/cm2)$ giving a squared residual over $r^2 = 98\%$ at a temperature of $70.0°C$.

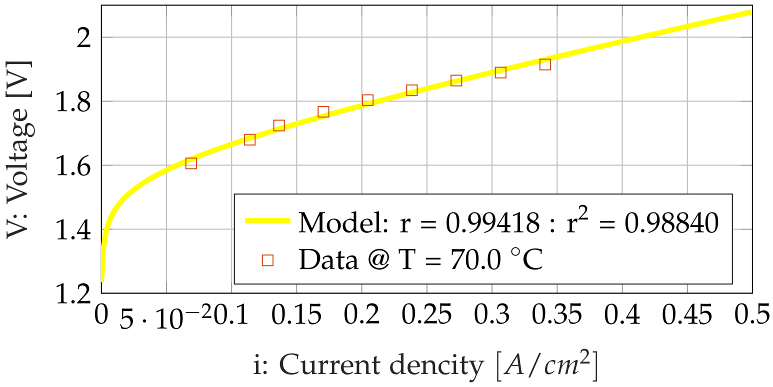

Figure 3.8: Model fitted to measured polarization curve at $T = 70.0°C$.

Because the exchange current densities are not constant with temperature they will be estimate using Equation 3.41.

$$i_{0,cat}(T\{°C\}) = 4.10828757 \cdot 10^{-8} \cdot 1.1333196^{T\{°C\}} \tag{3.41}$$

With the performance model fitted the cell potential can now be estimated at any temperature and current density. In Figure 3.9 polarization curves at temperatures between $20°C$ and $100°C$ calculated with the model is shown.

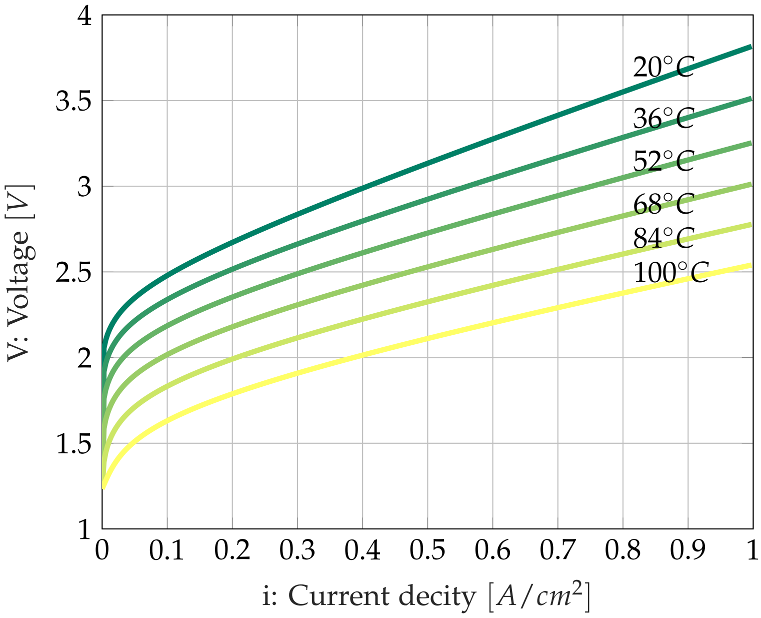

Figure 3.9: Extrapolated polarization curves at temperature between 20°C and 100°C.

Chapter 4

Heat Balance

Since the static performance of AWE is dependent on the operating temperature the following chapter will focus on the heat balance of the system. In this chapter the heat balance of the AWE stack will be described in three parts the heat generated in the cell stack, the heat lost to the surrounding from the stack and the heat removed from the stack by the circulation of electrolytes. The heat balance will consider the AWE stack as a lumped system which means the temperature gradient of the stack is assumed spatially uniform. This is done to simplify the otherwise complex differential heat equations needed to calculate the temperature distribution and heat transfers. At the end of the chapter, a description of the method used for temperature regulation of the AWE stack with a heat exchanger will be given.

The Heat balance of a lumped system is expressed as shown in Equation 4.1. Here the change in temperature over time is expressed by the sum of heat added to the system Q_i minus the sum of heat flowing out of the system Q_o divided by the total heat capacity of the system C_{tot}. For the AWE stack heat is added to the system through the heat generated by the water-splitting process Q_{loss}. Heat is then removed by convection and radiation through Q_{amb}. Heat is also removed by the flow of electrolyte Q_{liq}. The overall Heat balance of the AWE stack is then described by Q_{loss}, Q_{amb}, Q_{liq} and C_{tot} shown in Equation 4.2.

$$\frac{dT}{dt} = \frac{\sum Q_i - \sum Q_o}{C_{tot}} \tag{4.1}$$

$$\frac{dT}{dt} = \frac{Q_{loss} - Q_{liq} - Q_{amb}}{C_{tot}} \tag{4.2}$$

The overall heat capacity of the stack is calculated using Equation 4.3 where C_{tot} is shown to be the sum of the product between the mass and specific heat capacity of each component. In Table 4.1 a list of the different components of the stack is given along with their properties used for the calculation of the overall heat capacity of the stack. The values in Table 4.1 are taken from [Sakas et al. 2022].

$$C_t = \sum V^i \rho^i C_P^i = \sum L^i A_{Cell} \rho^i C_P^i \tag{4.3}$$

	Material	ρ	C_p	L
		$[kgm^{-}3]$	$[kJkg^{-}1K^{-}1]$	$[mm]$
Electrolyte space	Lye	1280	4.07	4.75
Diaphragm	Zirfon™	1	3.00	0.50
Bipolar plate	Steel	8000	0.42	6.50
Coating	Ni-Co	8900	$0.45 - 0.42$	a/a

Table 4.1: Material properties of AWE cell, including, density ρ, specific heat capacity C_p and thickness L.

4.1 Heat generated: Q_{loss}

The heat generated Q_{loss} can be expressed by the difference in cell potential U_{cell} and the thermal neutral potential U_{tn} shown in Equation 4.4. Here it is also shown that the heat is linearly proportional to the current used by an AWE cell I_{cell} and the number of cells in the stack E_c.

$$Q_{loss} = (U_{cell} - U_{tn}) \cdot I_{cell} \cdot E_c \tag{4.4}$$

Expanding the cell potential U_{cell} into the reversible potential U_{rev}, the overpotentials U_{act} and U_{act} helps to understand where the heat originates from. In Equation 4.5 it can be seen that heat is partly generated from the overpotentials U_{act} and U_{act}. The rest is from the difference in reversible and thermal neutral potential.

$$Q_{loss} = (U_{rev} + U_{act} + U_{ohm} - U_{th}) \cdot I_{cell} \cdot E_c \tag{4.5}$$

The thermal neutral potential U_{tn} is defined similarly to the reversible potential U_{rev} with the Nernst equation but using enthalpy instead of Gibbs free energy. In Equation 4.6 the thermal neutral potential U_{tn} at standard condition is shown.

$$U_{tn}^0 = \frac{\Delta H_{ref}^0}{z \cdot F} = 1.482[V] \tag{4.6}$$

In Equation 3.3 the relation between the thermodynamic potentials, enthalpy and Gibbs free energy is given by the change in entropy. Subtracting Equation 4.6 from 3.6 it can be shown In Equation 4.7 that the difference in U_{rev} and U_{tn} is the heat associated with the change in entropy also referred to as the reversible heat. [Lamy and Millet 2020]

$$U^0_{rev} - U^0_{th} = \frac{-T \cdot \Delta S^0_{ref}}{z \cdot F} = -0.253[V] \tag{4.7}$$

4.2 Heat lost to the surroundings: Q_{amb}

The heat lost to the surrounding Q_{amb} is summarised in Equation 4.8 and is shown to be composed of convection and radiation.

$$Q_{amb} = Q_{rad} + Q_{conv} \tag{4.8}$$

The convective heat transfer is formulated as shown in Equation 4.9 where h is the effective heat transfer coefficient, A_{stack} the surface area of the AWE stack, T_{stack} is the operating temperature and T_{amb} the ambient temperature.

$$Q_{conv} = hA_{stack}(T_{stack} - T_{amb}) \tag{4.9}$$

It is assumed that the stack consist of a circular cell and the surface area is therefore calculated as the area of a cylinder. Assuming the stack is lying horizontally a numerical function presented in Equation 4.10 for the heat transfer coefficient can be used to estimate the size of h depending on the temperature difference and the diameter of the cells.

$$h = 1.32 \left(\frac{T_{stack} - T_{amb}}{D} \right)^{1/4} \tag{4.10}$$

The heat radiating from the stack to the surroundings can be derived from Stefan Boltzmann's law and the reciprocity rule for view factors seen in Equation 4.11 where e is the emissivity of the grey body. It is assumed that the stack behaves like a black body and e is therefore simple unity.

$$Q_{rad} = \sigma A_{stack} e (T^4_{stack} - T^4_{amb}) \tag{4.11}$$

4.3 Heat removed by the flow of electrolyte: Q_{liq}

The last heat flow in the overall heat balance 4.2 is the heat removed by the flow of electrolyte Q_{liq}. In Equation 4.12 Q_{liq} is shown to be estimated by the mass flow of electrolyte $\dot{m}_{ele,i}$, the specific heat capacity of electrolyte and the difference in temperature between the AWE stack temperature T_{stack} and the temperature of the electrolyte entering the stack $T_{ele,i}$.

$$Q_{liq} = \dot{m}_{ele,i} \cdot C_{P,ele} \cdot (T_{stack} - T_{ele,i}) \tag{4.12}$$

For the mass flow of electrolyte, $\dot{m}_{ele,i}$ a fixed estimate will be used. In [Kojima et al. 2018] it was shown that the flow rate of electrolyte is proportional to the capacity of the AWE system and a ratio was given. Using the ration giving in [Kojima et al. 2018] and multiplying with the highest power draw calculated with the static performance model operating at a maximum allowed current density of $i_{cell} = 0.6A/cm^2$ at 80°C a mass flow rate around $\dot{m}_{ele,i} = 30kg/s$ was found.

The specific heat capacity of electrolyte $C_{P,ele}$ is calculated using a polynomial fitted to data from a model by [Laliberté 2009] relating it to the morality of KOH in the electrolyte C_{KOH} and temperature. The temperature of the electrolyte entering the stack $T_{ele,i}$ will depend on what happens to the electrolyte leaving the stack $T_{ele,o}$. On the anode side, it is assumed oxygen is simply separated from the electrolyte changing the mass flow but not the temperature. On the cathode side, hydrogen is separated and feedwater is added thereby cooling the electrolyte. In Equation4.13 an expression for the temperature of the electrolyte after adding feed water is given.

$$T_{ele} = \frac{\dot{m}_{ele,o} \cdot C_{P,ele} \cdot T_{ele,o} + \dot{m}_{H_2O,feed} \cdot C_{P,water} \cdot T_{H_2O,feed}}{\dot{m}_{ele,o} \cdot C_{P,ele} + \dot{m}_{H_2O,feed} \cdot C_{P,H_2O}} \tag{4.13}$$

Because the feedwater is added to make up for the hydrogen and oxygen produced the mass flow of feed water can be calculated using Faraday's law shown in Equation 4.14. Here $\varepsilon_{faradaic}$ is the faradaic efficiency, A_{cell} is the area of a cell, M_{H_2O} is the molar mass of water, z is the number of molecules of interest produced or consumed per reaction, F is faradays constant and E_c is the number of cells. Since one molecules of water is consumed per reaction shown in Table 1.1 $z = 1$.

$$\dot{m}_{H_2O,feed} = \varepsilon_{faradaic} \left(\frac{i_{cell} A_{cell} \cdot M_{H_2O}}{zF} \right) E_c \tag{4.14}$$

Most cooling of the electrolyte is how ever done by the heat exchanger. A description of how the heat exchanger is modelled is therefore given next.

4.4 Heat exchanger

To model the heat exchanger the Number of Transfer Units (NTU) method also referred to as the effectiveness method will be used since all inlet and outlet temperatures are not known. In Figure 4.1 a counter-flow heat exchanger is illustrated and it is shown where the different temperatures flow in and out. The temperatures are labelled with two letters the first referring to the fluid "h" for hot, electrolyte or lye and "c" for cold or water. The second letter denotes whether the temperature is at an inlet "i" or outlet "o".

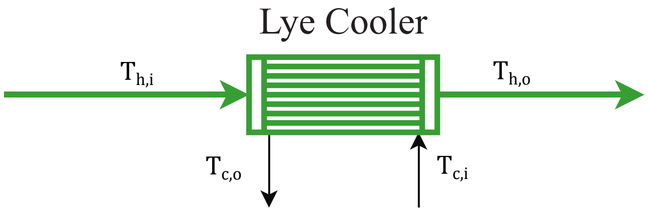

Figure 4.1: Diagram of a counter flow heat exchanger.

First energy conservation is enforced between the two streams in Equation 4.15 and 4.16 ensuring that heat lost from the cold stream is equal to the heat gained by the cold stream.

$$q = \dot{m}_h C_{P,ele}(T_{h,i} - T_{h,o}) \tag{4.15}$$

$$q = \dot{m}_c C_{P,H_2O}(T_{c,i} - T_{c,o}) \tag{4.16}$$

An effectiveness coefficient ϵ is proposed to tell how effective the heat exchanger is by taking the ratio between the heat transfer achieved q and the highest possible heat transfer q_{max}.

$$\epsilon = \frac{q}{q_{max}} \tag{4.17}$$

In Equation 4.18 the highest possible heat transfer q_{max} is formulated as the temperature difference between the inlet hot $T_{h,i}$ and cold stream $T_{c,i}$ multiplied by C_{min}. C_{min} is the lowest heat capacity of the two streams and is found as shown in Equation 4.19 by evaluating which of the product between mass flow and specific heat capacity is lower between the hot and cold stream. C_{max} The highest heat capacity is found similarly shown in Equation 4.20 and used later on in the NTU method.

$$q_{max} = C_{min}(T_{h,i} - T_{c,i}) \tag{4.18}$$

$$C_{min} = min(\dot{m}_h C_{P,ele}, \dot{m}_c C_{P,H_2O}) \tag{4.19}$$

$$C_{max} = max(\dot{m}_h C_{P,ele}, \dot{m}_c C_{P,H_2O}) \tag{4.20}$$

For a counterflow heat exchanger, the effectiveness coefficient is formulated as in Equation 4.21. Here C_r is the ratio C_{min} to C_{max} shown in Equation 4.22 and NTU is the number of heat transfer unit as calculated shown in Equation 4.23. In the formulation for NTU is the overall heat transfer coefficient set to $h = 60(W/m^2K)$ and A is the area of the heat exchanger. For the model, the area was calculated so that the heat exchanger was capable of cooling the AWE stack operating at maximum load with a mass flow of cooling water of 90% of the electrolyte flow with a cold inlet temperature of $20°C$ resulting in an area of $1550(m^2)$.

$$\epsilon = \frac{1 - \exp(-NTU(1 - C_r))}{1 - Cr\exp(-NTU(1 - C_r))} \tag{4.21}$$

$$C_r = \frac{C_{min}}{C_{max}} \tag{4.22}$$

$$NTU = \frac{h\,A}{C_{min}} \tag{4.23}$$

4.5 P Controller

To keep the AWE stack at a constant operating temperature T_{ref} the mass flow of cooling water $\dot{m}_{H2_O,cooling}$ is controlled using a simple feedback loop with a proportional gain P shown in Figure 4.2. Running through the control loop six operations are made. First The temperature difference between the reference temperature T_{ref} and the temperature of the electrolyte exiting the electrolyte mixer is calculated and used as the error. The error is then multiplied by a proportional gain P. The control signal is then limited by a saturation limited between $0kg/s$ and a mass flow 10% above what is needed to keep the AWE stack cooled at $80°C$ under full load with the heat exchanger dimensioned previously. Then the control signal is rate limited to include ramping rate of the pump. The ramping was chosen to be 20% a second of the maximum flow rate of the pump. The control signal is then used as the mass flow of cooling water and $T_{h,o}$ can be calculated using the NTU method. lastly $T_{h,o}$ is fed back into the plant and a new stack temperature is calculated.

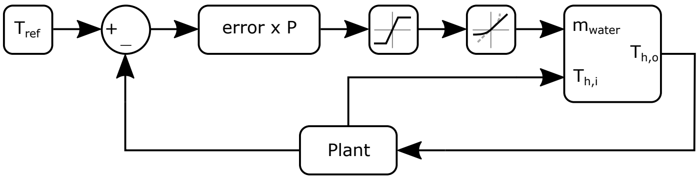

Figure 4.2: Feedback P control diagram with saturation and rate limiter.

With the temperature control system in place the model has all the equations needed to describe the performance of the AWE system. In the following chapters the the modeled performance of the AWE system will be shown under different modes of operation.

Chapter 5

System dynamics

5.1 Dynamic response to current step

To ensure the performance of the AWE system responds as expected, the model will be subjected to a synthetic step input at an operating temperature of $80°C$. The step is defined in current density from the minimum allowed of $i_{min} = 0.1(A/cm^2)$ to the maximum of $i_{max} = 0.6(A/cm^2)$ shown in Figure 5.1 where the corresponding DC power consumption is shown as well. The power consumption is calculated from the input current density i_{cell}, the cell potential U_{cell} and the total area of the AWE stack as shown in Equation 5.1.

$$Power_{Stack} = i_{cell} U_{cell} \pi \frac{D^2}{4} E_c \tag{5.1}$$

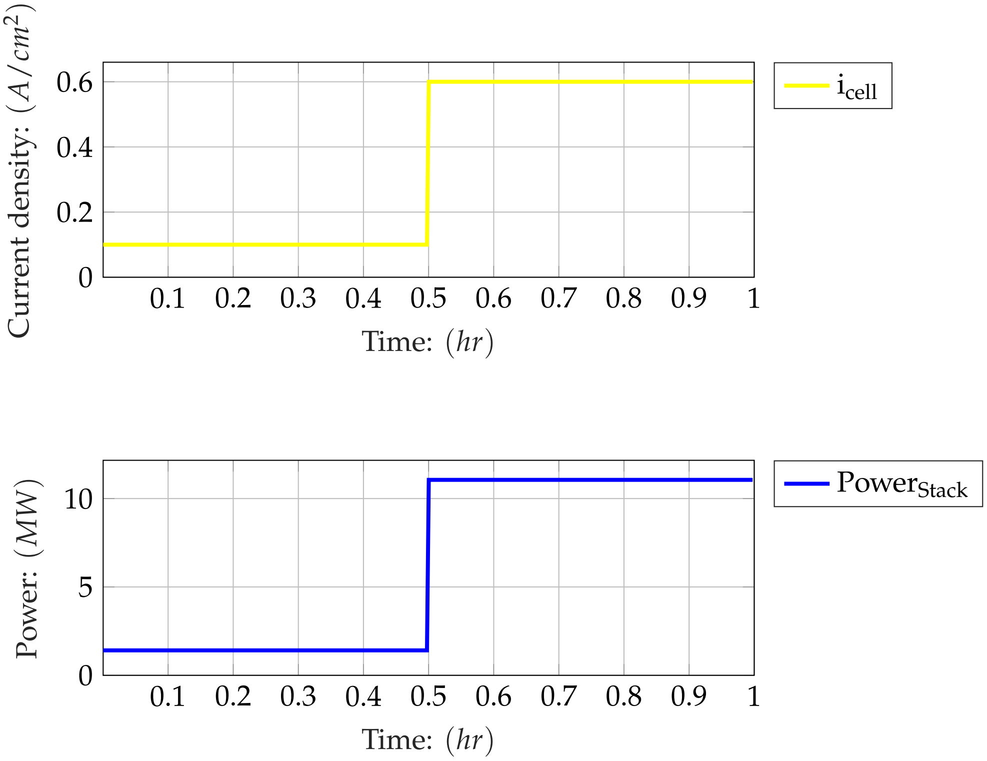

Figure 5.1: Current density step input from $i_{min} = 0.1(A/cm^2)$ to $i_{max} = 0.6(A/cm^2)$ and the Corresponding power consumption of the AWE stack.

In Figure 5.2 the cell potential U_{cell}, Reversible potential U_{rev}, the two over potentials U_{act} and U_{ohm} for activation and ohmic losses respectively and the thermal neutral potential U_{tn} is shown. It can be seen between Figure 5.1 and 5.2 that the potentials follows the the current, which is the expected result from an AWE cell supported by experimental result. In the article [Shen et al. 2018] experiments was conducted to find dynamic power characteristics of an AWE stack rated at $20(kW)$ here is was shown the the cell potential followed the current with a lag of less than $1(ms)$. The cell potential in Figure 5.2 does also lined up with the potential previously found in the polarization curve shown the in Figure 3.9 with $U_{cell} = 1.6V$ at $0.1A/cm^2$ & $80°C$ and $U_{cell} = 2.1V$ at $0.6A/cm^2$ & $80°C$.

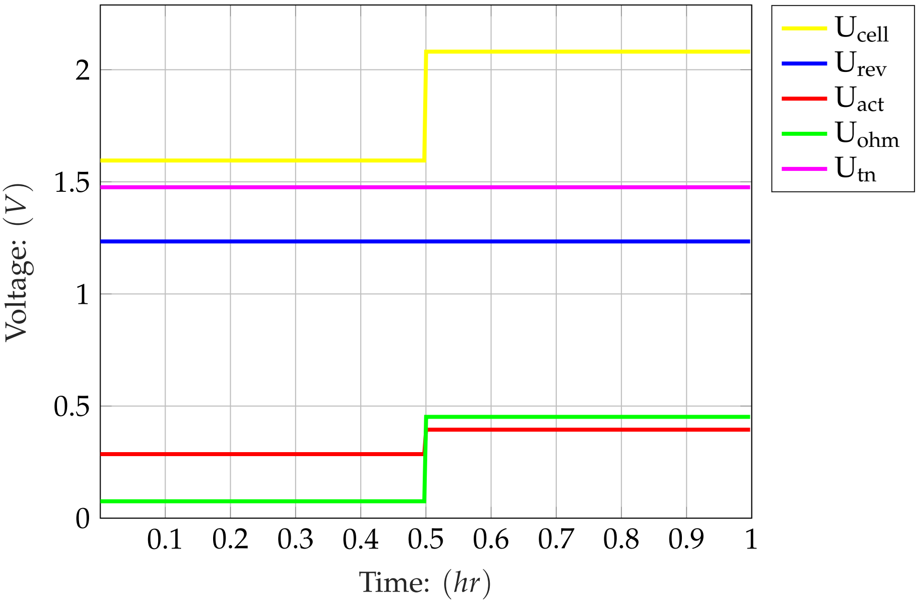

Figure 5.2: Dynamic response of cell potential U_{cell} and over potentials U_{act} and U_{ohm} to current step.

In Figure 5.3 the temperature of the AWE stack T_{stack} and the electrolyte cooled by the heat exchanger entering the stack $T_{ele,i}$ is shown. The temperature of the stack T_{stack} can be seen to start initially at $80°C$ and is kept there by the controller. In Figure 5.4 the mass flow of cooling water $\dot{m}_{H_2O,cooling}$ can be seen to be very low initially at $\dot{m}_{H_2O,cooling} = 0.1kg/s$ under the current density of $i_{min} = 0.1A/cm^2$. This is explained by the low heat generated in the AWE stack of $Q_{loss} = 0.1MW$ and the relatively high heat being lost to the surroundings $Q_{amb} = 53.3kW$ seen in Figure 5.5. Additionally, the high heat loss to the surroundings Q_{amb} is shown to be constant as it only varies with the temperature of the AWE stack which is held constant by the controller. This leaves only $52.3kW$ to be cooled by the heat exchanger and is the lowest value of Q_{liq} expected apart from when the AWE stack is heating up and when the system is not producing hydrogen. Also worth observing from the three Figures 5.3, 5.4 and 5.5 is that at no point is the system losing more heat than it is producing. Therefore heating the system under operation is not needed to keep the system at a higher efficiency.

When the current density goes from $i_{min} = 0.1A/cm^2$ to $i_{max} = 0.6A/cm^2$ the mass flow of cooling water can also be seen to step up from $\dot{m}_{H_2O,cooling} = 0.1kg/s$ to $\dot{m}_{H_2O,cooling} = 24.0kg/s$ almost instantaneously as the pump is only rate limited to 20% a second as mentioned earlier in the controller section 4.5. This means the mass flow of cooling water can go from 0% to 100% in 5 seconds, this is shorter than some of the time scales of the system. The temperature of the electrolyte entering the stack $T_{ele,i}$ is seen In Figure 5.3 to follow the same fast dynamics as the mass flow of cooling water. This is due to the inherently non-dynamic nature of the NTU method making the temperature control of the AWE stack practical instantaneous. More realistically there would be a delay between the change in mass flow rate of cooling water $\dot{m}_{H_2O,cooling}$ and the change of outlet temperature of heat exchanger $T_{ele,i}$ missing from the model. Including this delay would make the Q_{liq} lack behind Q_{loss} in Figure 5.5 possibly leading to an overshoot in stack temperature T_{stack} making the need for the small oversizing of the cooling solution made in the model. Due to the nature of the P controller implemented a small constant error can not be avoided. The error is include in Figure 5.3 but is barely visible as the temperature goes from $T_{stack} = 80.000°C$ to $T_{stack} = 80.009°C$. The error is much smaller than any real temperature control could achieve due to numerous resounds one being measuring uncertainties higher than the error.

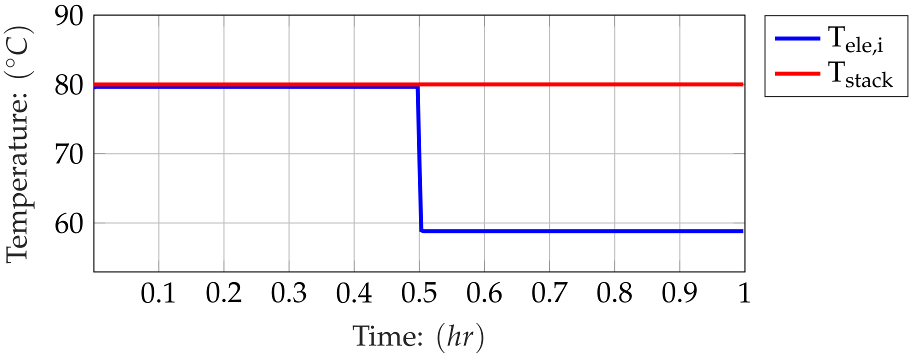

Figure 5.3: Dynamic response of stack temperature T_{stack} and temperature of electrolyte entering $T_{ele,i}$ to current step.

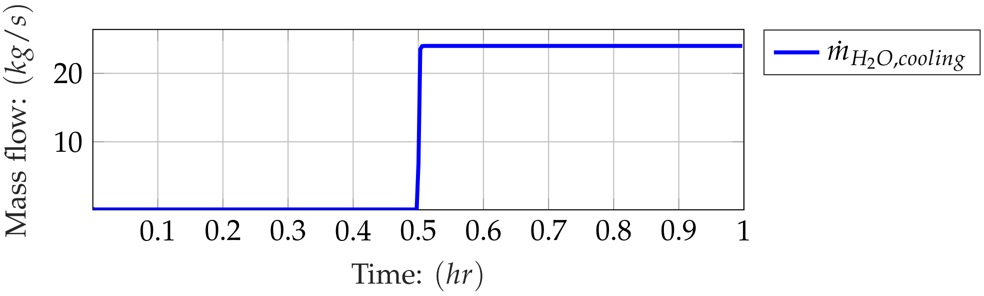

Figure 5.4: Dynamic response of mass flow of cooling water $\dot{m}_{H_2O,cooling}$ in heat exchanger to current step.

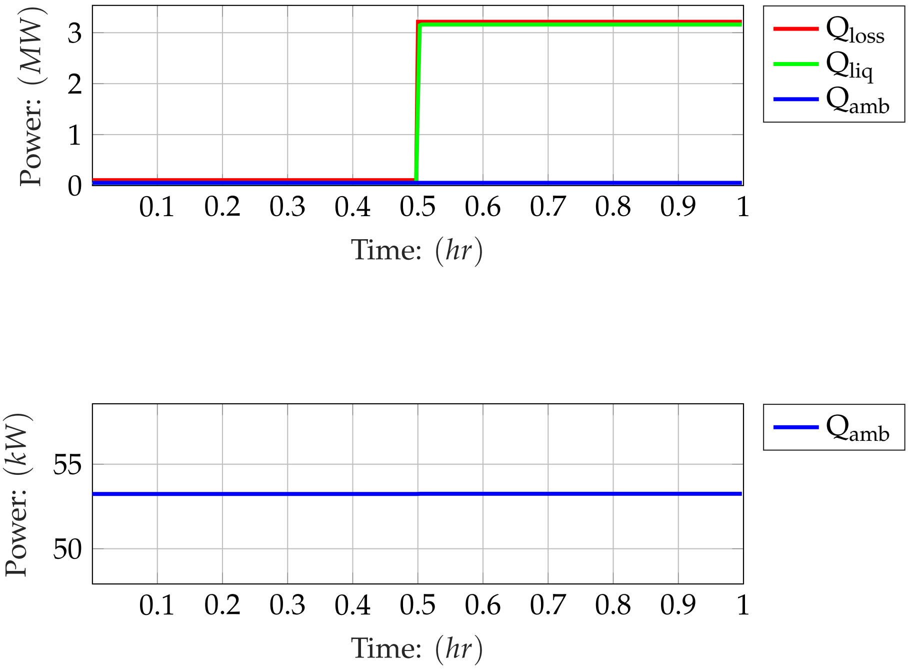

Figure 5.5: Dynamic response of heat flows Q_{loss}, Q_{liq} and Q_{amb} to current step.

The efficiency of the AWE stack is shown in Figure 5.6 to be in the range between $\varepsilon_{cell} = 80.3\%$ and $\varepsilon_{cell} = 63.5\%$ at $80°C$ in the range of current density.

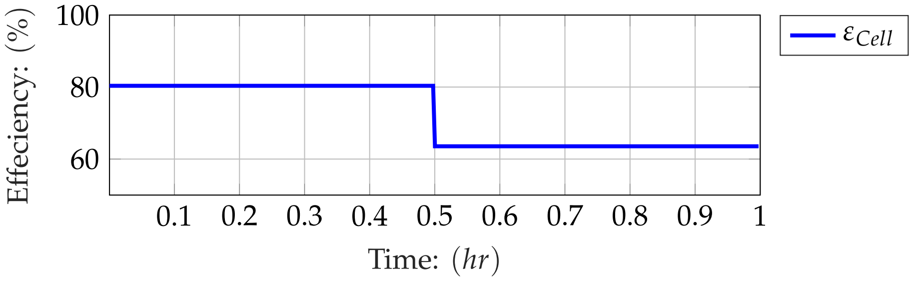

Figure 5.6: Dynamic response of energy efficiency ε_{cell} to current step.

5.2 Dynamic heating process

Next, the heating process of the system is tested. The AWE stack temperature is set to an initial value of $T_{stack} = 20°C$ seen in Figure 5.9. Initially, no current is applied to see if everything keeps unchanging as expected. The current is kept turned off for half an hour and as can be seen in Figure 5.8 to 5.11 every parameter is unchanging as expected. After half an hour the current density is set the maximum value of $i_{max} = 0.6A/cm^2$. In Figure 5.7 the power can be seen to start high at $Power_{cell} = 12.2MW$ and slowly fall to a lower and steady value of $Power_{cell} = 11.1MW$. This is because the power is not only proportional to the current density but also the cell potential U_{cell}.

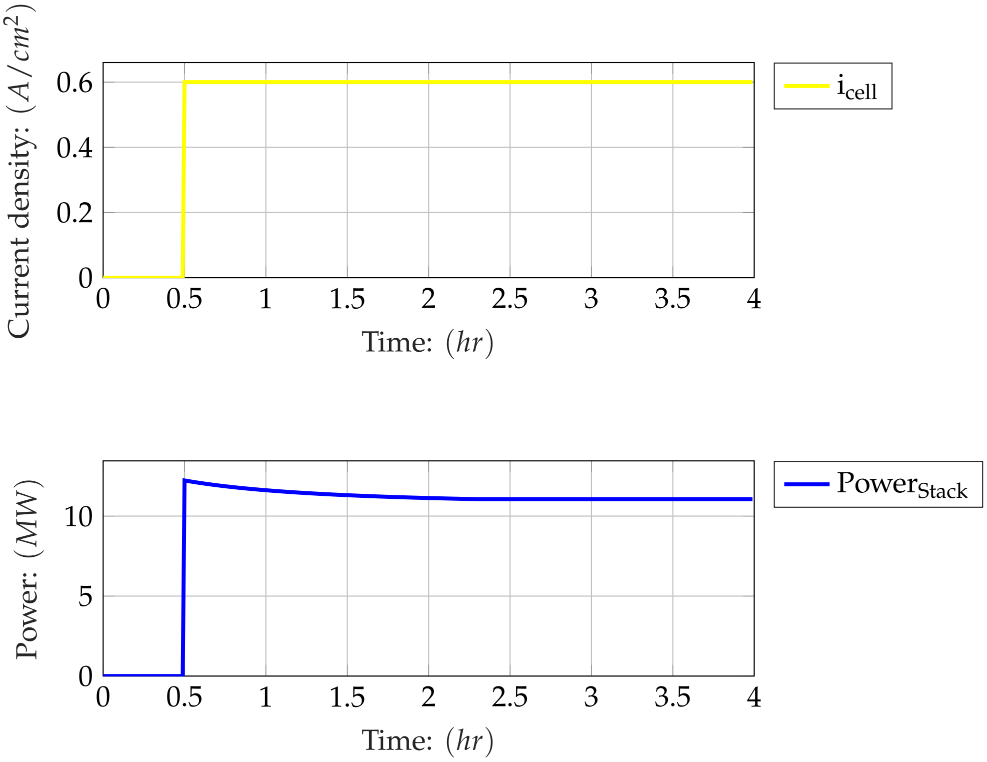

Figure 5.7: Current density and the Corresponding power consumption of the AWE stack in the heating process.

In Figure 5.8 it is shown that the potential of the cell start high at $U_{cell} = 2.3V$ and slowly fall to a lower and steady value of $U_{cell} = 2.1V$ giving the shape of the power curve in Figure 5.7. The initial high power consumption and cell potential can be seen the originate from the ohmic over potential U_{ohm}. This can be explained by the lower specific conductivity of the electrolyte at lower temperatures shown in Figure 3.4. As the temperature increases the conductivity of the electrolyte does as well and the ohmic overpotential decreases. The activation over potential U_{act} is shown to increasing over time as it is proportional to temperature. The increase is however outweighed by the decrease in U_{ohm}.

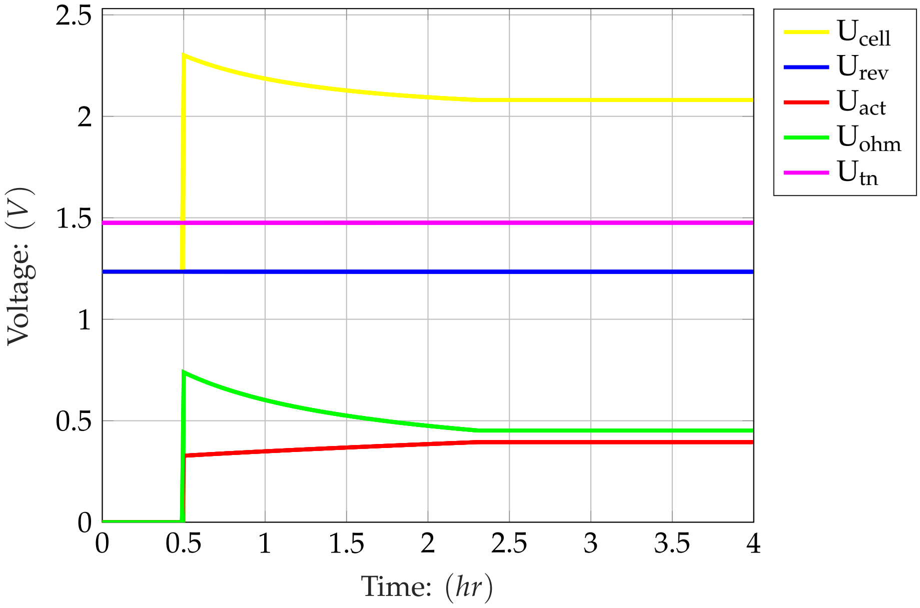

Figure 5.8: Dynamic response of cell potential U_{cell} and over potentials U_{act} and U_{ohm} in the heating process.

In Figure 5.9 the rise in temperature over time is shown. It can be seen that it take 1.5 hours for the system to heat up from 20°C to 80°C under maximum load. Looking closely as temperatures in Figure 5.9 it can be seen that $T_{ele,i}$ is slightly lower than the stack temperature T_{stack}. This could be caused by the addition of feed water in the hydrogen electrolyte separator. This also explains why the temperature difference increasing.

It is shown that as the temperature increases the rate of change in temperature decreases as expected. This is mainly because of the decrease in heat generated Q_{loss} over time shown In Figure 5.10. The reason for the decrease in Q_{loss} can be seen in Figure 5.8 and Figure 5.11 as the efficiency of the AWE stack is shown to increase with the temperature wasting less energy to heat. Another reason why the the rate of change in temperature decreases is that the heat lost to the surroundings increases with temperature shown in Figure 5.10. This effect is how ever small compared the decrease in Q_{loss}.

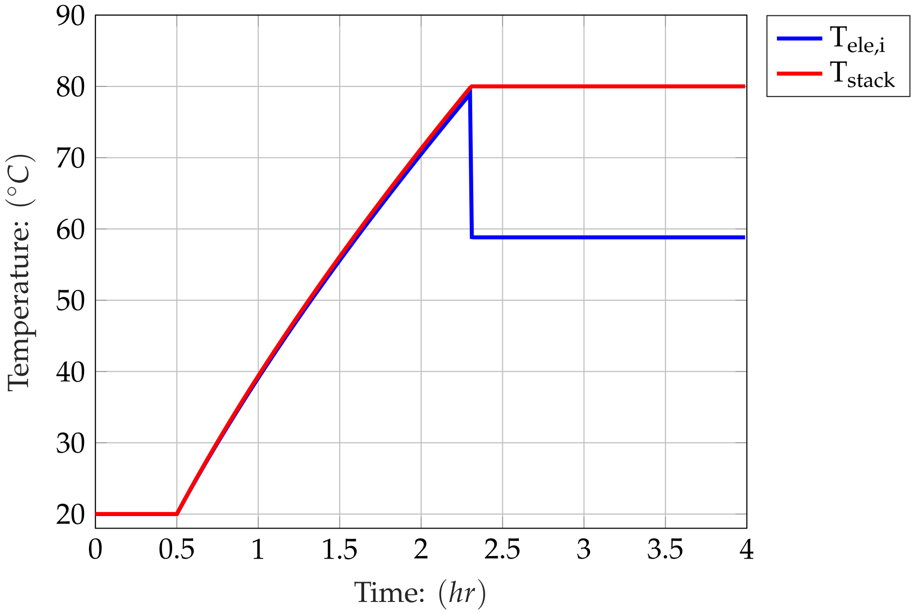

Figure 5.9: Dynamic response of stack temperature T_{stack} and temperature of electrolyte entering $T_{ele,i}$ in the heating process.

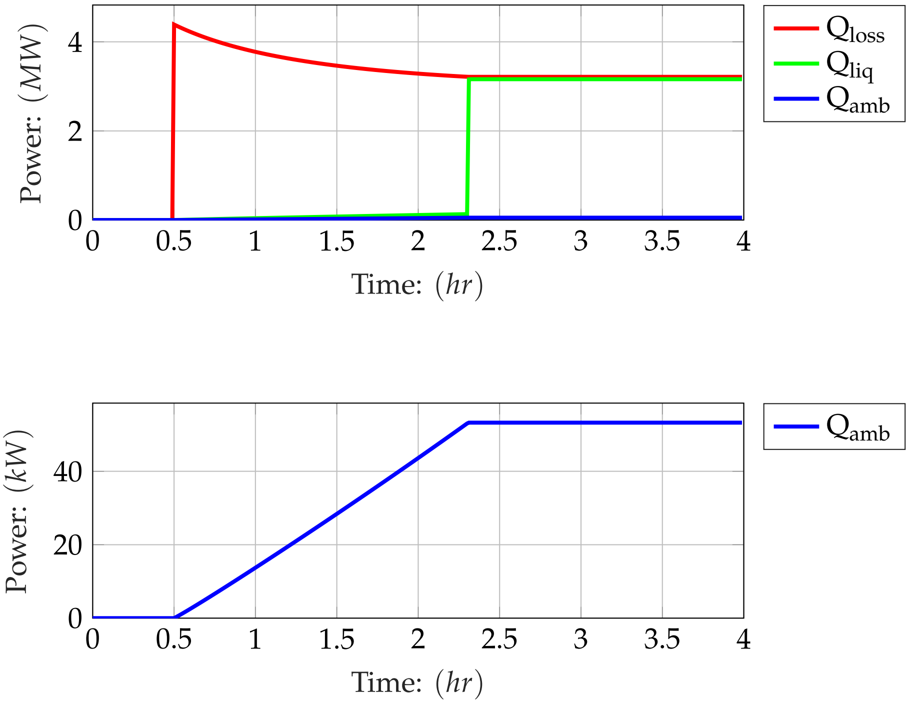

Figure 5.10: Dynamic response of heat flows Q_{loss}, Q_{liq} and Q_{amb} in the heating process.

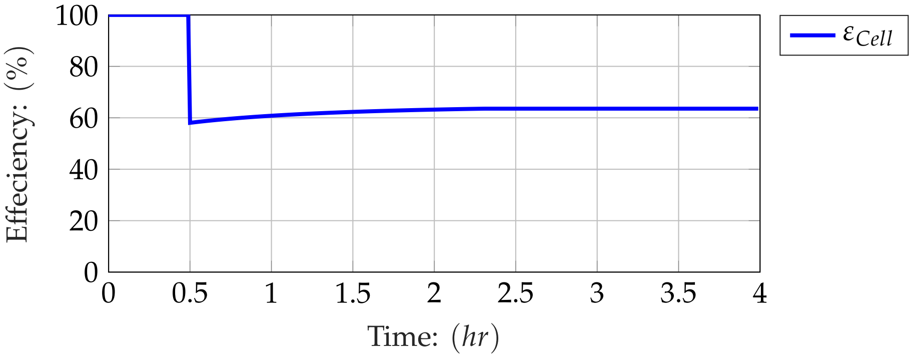

Figure 5.11: Dynamic response of energy efficiency ε_{cell} in the heating process.

Best illustrated in Figure 5.9 it is shown that the temperature controller is kept of until the temperature of the AWE stack reaches 80°C. At this point the mass flow of cooling water $\dot{m}_{H_2O,cooling}$ ramps up seen in Figure 5.12, The temperature $T_{ele,i}$ decreases seen in Figure 5.9, the the cooling Q_{liq} increases seen in Figure 5.10 and all other parameters plateaus.

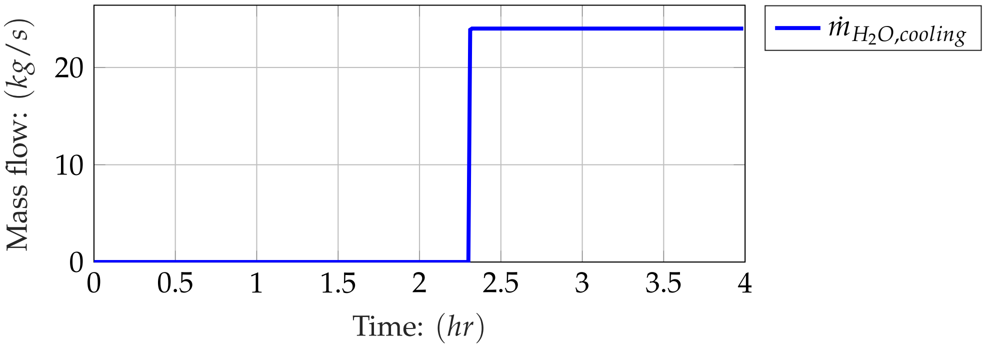

Figure 5.12: Dynamic response of mass flow of cooling water $\dot{m}_{H_2O,cooling}$ in heat exchanger in the heating process.

5.3 Dynamic cool down process

Using the AWE system in combination with IRES might include a period where no power is available. During these periods the system will slowly lose heat to the surroundings lowering the temperature of the stack and lowering the efficiency of the AWE stack for when power is available again. In Figure 5.13 the cool down process from 80°C to 20°C is shown. The system is initially operated with a constant load at 80°C for an hour and afterwards shut off. In Figure 5.14 the first 1.5 hour of operation is shown. In Figure 5.13 it can be seen that the cool down process is longer in orders of magnitude than the heat up process. The heat loss shown in Figure 5.15 is however not negligible as a 10°C temperature drop takes place within the first day when no power is available.

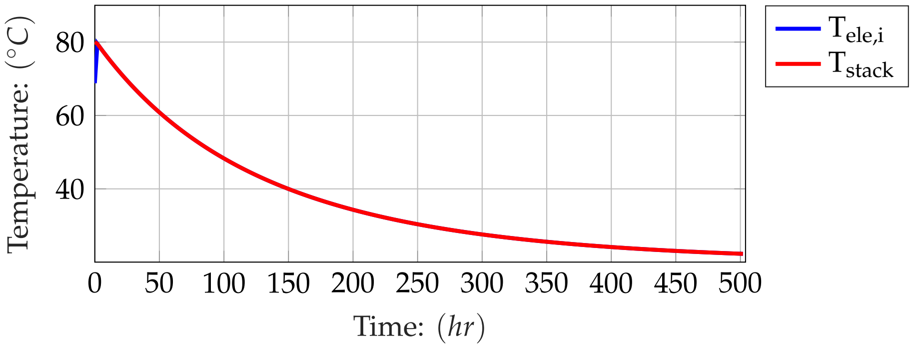

Figure 5.13: Dynamic response of stack temperature T_{stack} and temperature of electrolyte entering $T_{ele,i}$ in the cool down process.

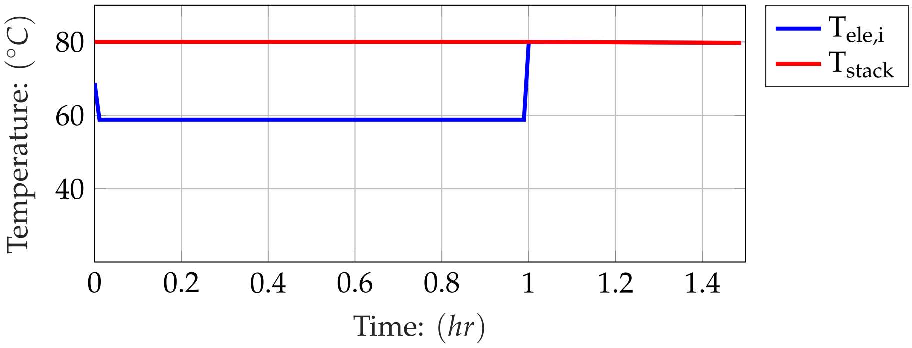

Figure 5.14: Initial first hour dynamic response of stack temperature T_{stack} and temperature of electrolyte entering $T_{ele,i}$ in the cool down process.

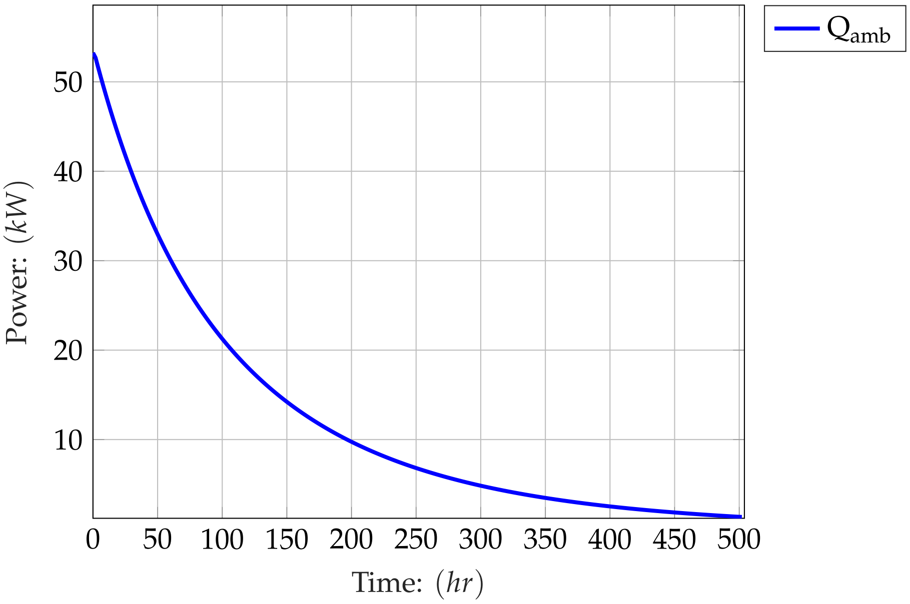

Figure 5.15: Dynamic response of Q_{amb} in the cool down process.

Chapter 6

System dynamics using Intermittent Renewable Energy Sources

6.1 Surplus from intermittent renewable energy sources

Having tested the performance of the AWE system under a synthetic load the following chapter will explore the system performance under a more realistic load. As mentioned at the begging of the report using AWE in combination with IRES could be a way of utilising the surplus energy of IRES. In Figure 6.1 the power produced by wind and solar from the United Kingdom in the month of April is shown.

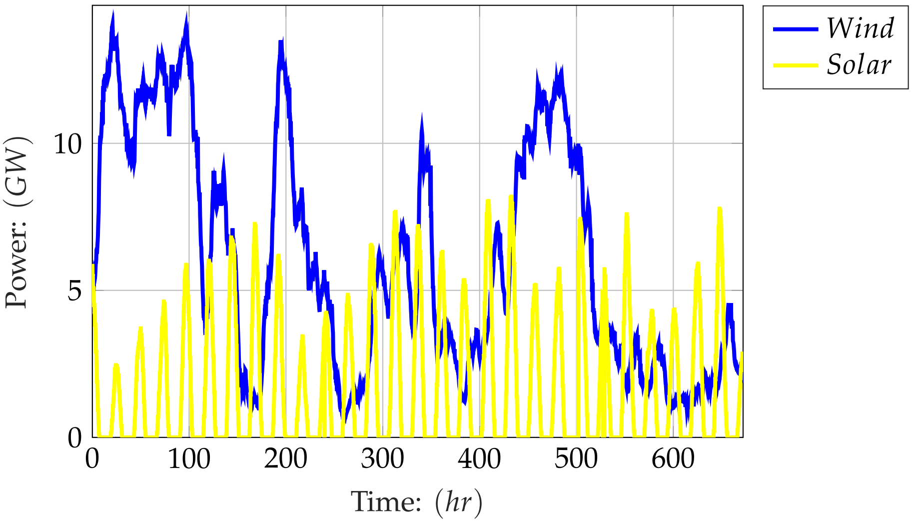

Figure 6.1: Wind and solar power production from the United Kingdom in the period between $2022-04-03-11:50$ and $2022-05-03-09:45$.

In Figure 6.2 the power demand of the United Kingdom is shown in the same period of time.

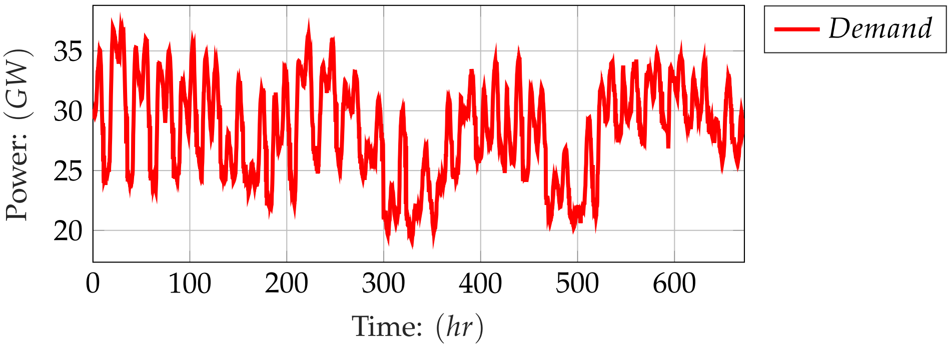

Figure 6.2: Power demand of the United Kingdom in the period between $2022-04-03-11:50$ and $2022-05-03-09:45$.

Subtracting the power demand from the produced power of wind turbines then shows the excess wind power if the grid was only getting energy from the wind turbines. This is shown in Figure 6.3 and here it can be seen that the United Kingdom has far less wind power than power consumption.

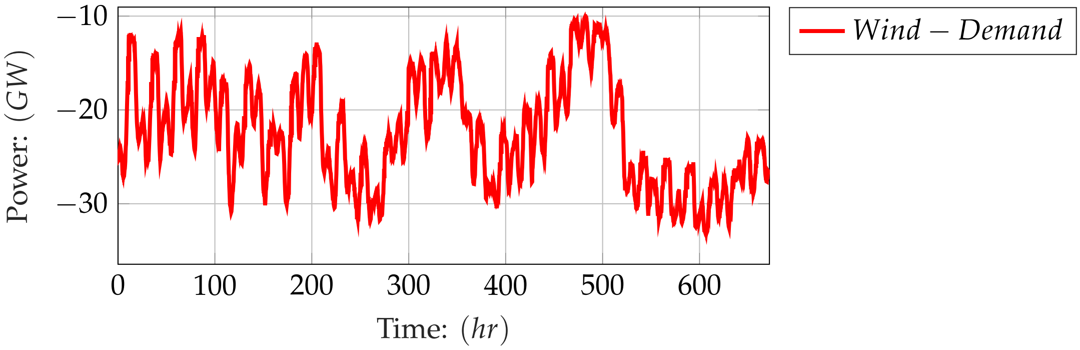

Figure 6.3: Wind power production subtracted by demand of the United Kingdom in the period between $2022-04-03-11:50$ and $2022-05-03-09:45$.

If the installed wind turbine capacity was three times larger than currently excess power production begins to occur shown in Figure 6.4 with excess power coloured green and deficit coloured red. It should be emphasized that this way of accessing surplus IRES power production is completely arbitrary and is done solely to create a realistic pattern of power production. In Figure 6.5 the excess power is isolated and shown.

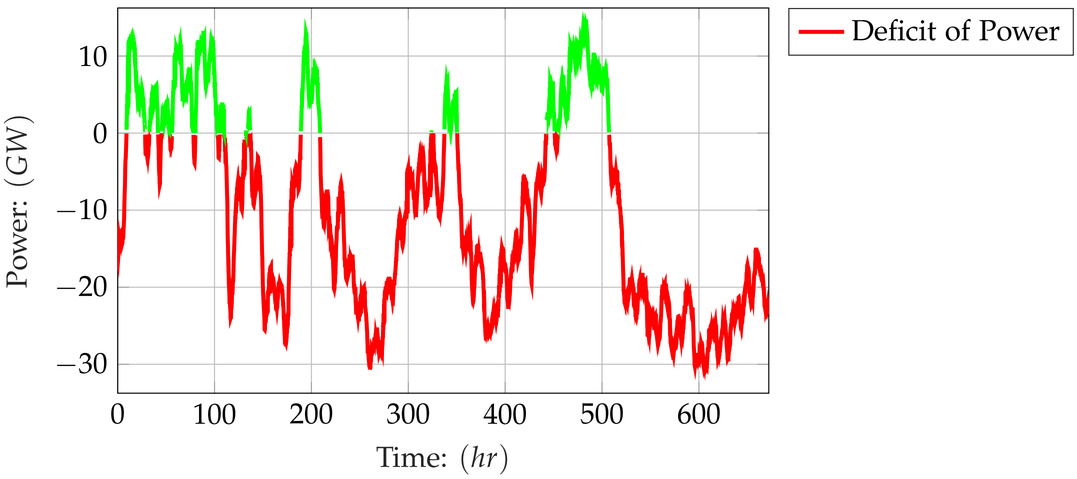

Figure 6.4: Excess wind power production shown in green and deficit of power shown in red.

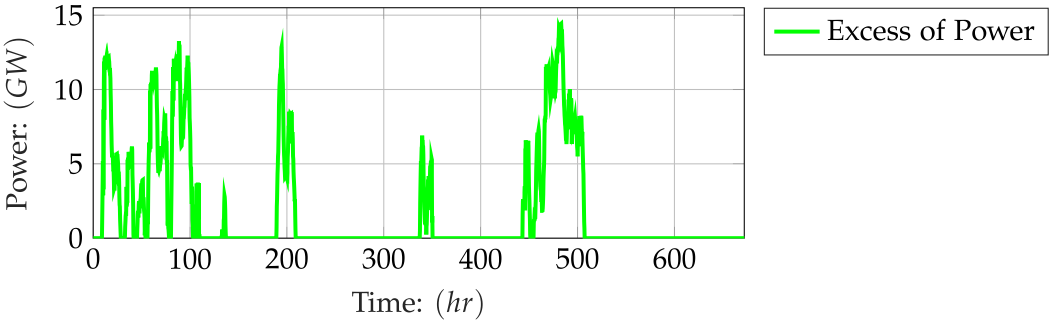

Figure 6.5: Excess wind power production.

The power production from the entire UK in this scenario is much more than a single AWE system can consume. Therefore the power is scaled down to the AWE modelled in this report.

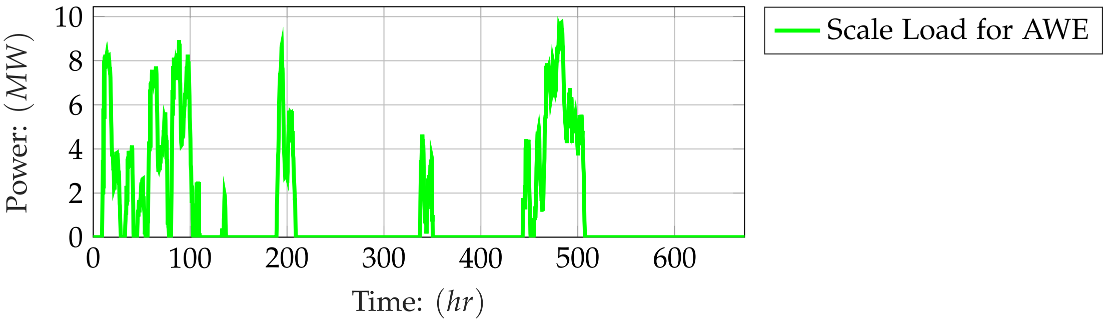

Figure 6.6: Excess wind power production scaled down to the capacity of the AWE system.

6.2 Dynamic respond to excess wind power

Using the excess power from wind turbines previously defined the current density, efficiency, temperatures, heat flows and potentials of the AWE stack is shown in the Figure 6.7,6.8 ,6.9, 6.10 and 6.11 respectively. Operation of the AWE system using this method a mean efficiency over the whole period is calculated to be $\varepsilon_{cell} = 73.9\%$. the mean efficiency coefficient is calculated after shorting out all values of $\varepsilon_{cell} = 100\%$ as the AWE stack is not producing any hydrogen and are therefore not relevant.

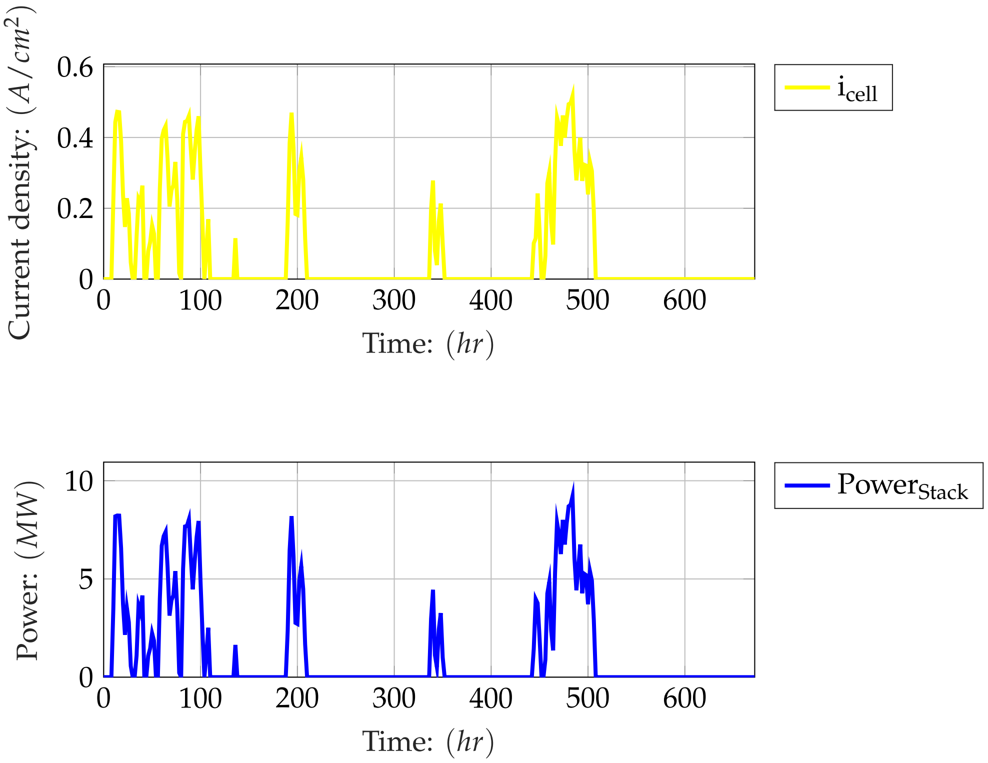

Figure 6.7: Power load and the corresponding current density of the AWE stack using excess wind power.

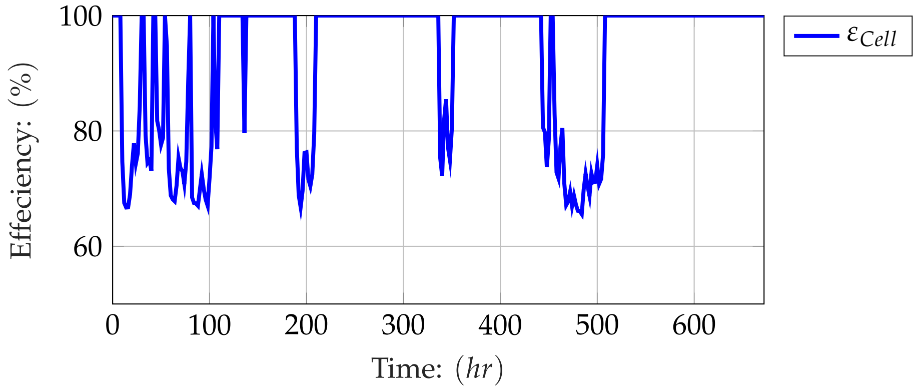

Figure 6.8: Dynamic response of the energy efficiency ε_{cell} when using excess wind power.

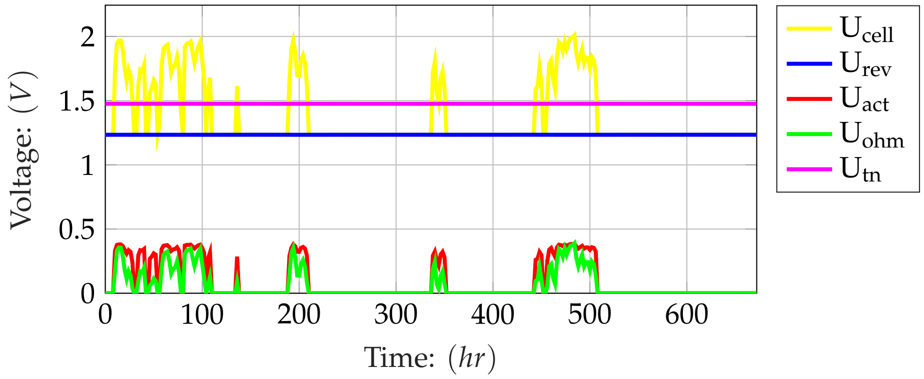

Figure 6.9: Dynamic response of cell potential U_{cell} and over potentials U_{act} and U_{ohm} when using excess wind power.

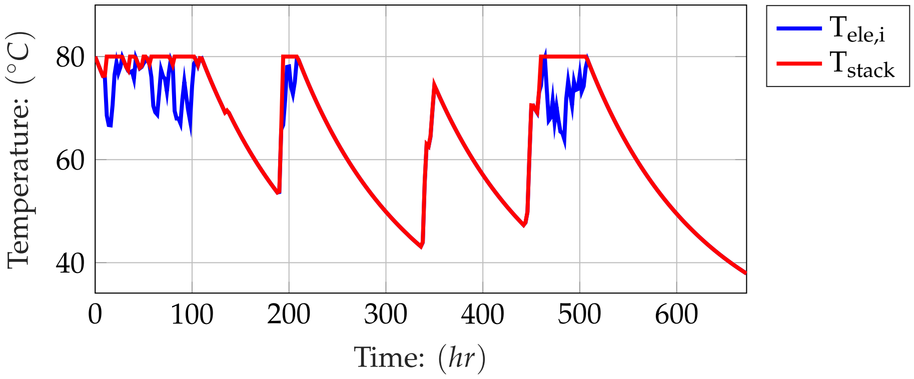

Figure 6.10: Dynamic response of stack temperature T_{stack} and temperature of electrolyte entering $T_{ele,i}$ when using excess wind power.

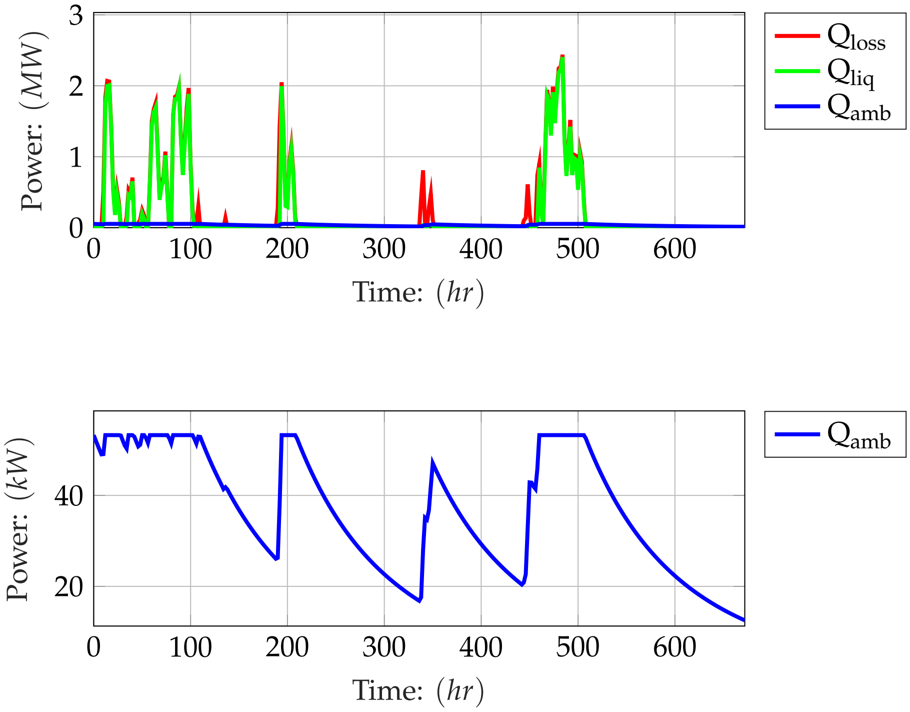

Figure 6.11: Dynamic response of heat flows Q_{loss}, Q_{liq} and Q_{amb} when using excess wind power.

6.3 Dynamic respond to excess solar power

Similar to the wind power production the AWE system was tested using solar power. Here the production of solar power was multiplied by 12 to have excess power. The current density, efficiency, potentials, temperatures and heat flows of the AWE stack is shown in the Figure 6.12, 6.13, 6.14, 6.15 and 6.16 respectively. Operation of the AWE system using solar power a mean efficiency over the whole period is calculated at $\varepsilon_{cell} = 75.1\%$. The mean efficiency coefficient is calculated in the same way as when using wind power by sorting out values of $\varepsilon_{cell} = 100\%$.

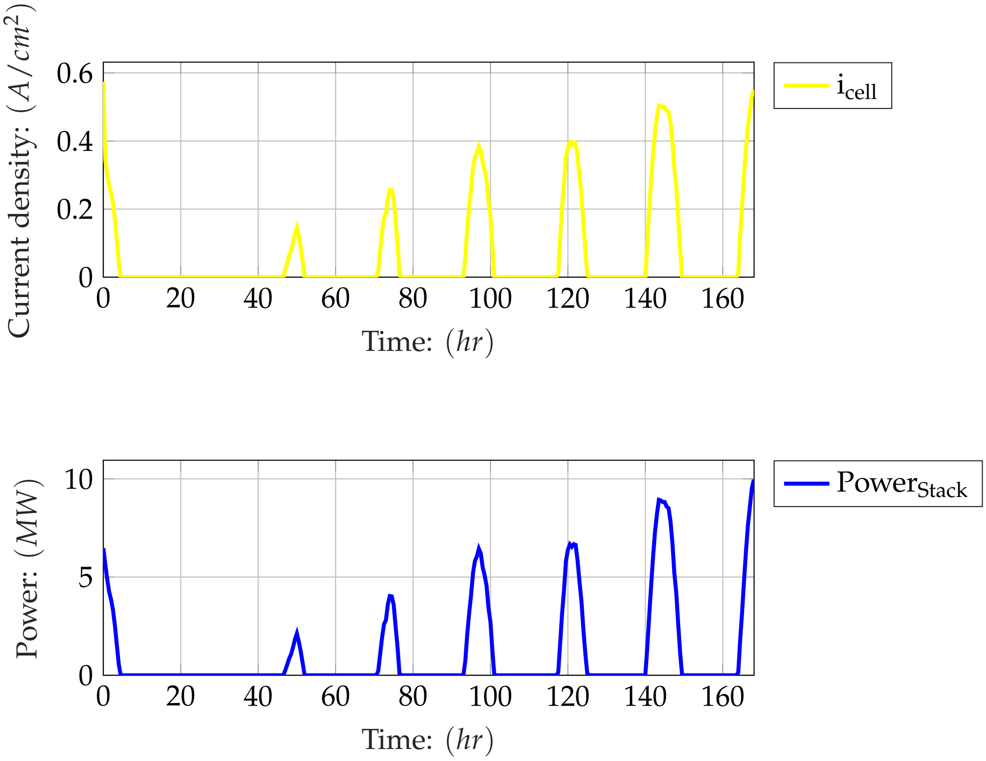

Figure 6.12: Power load and the corresponding current density of the AWE stack using excess solar power.

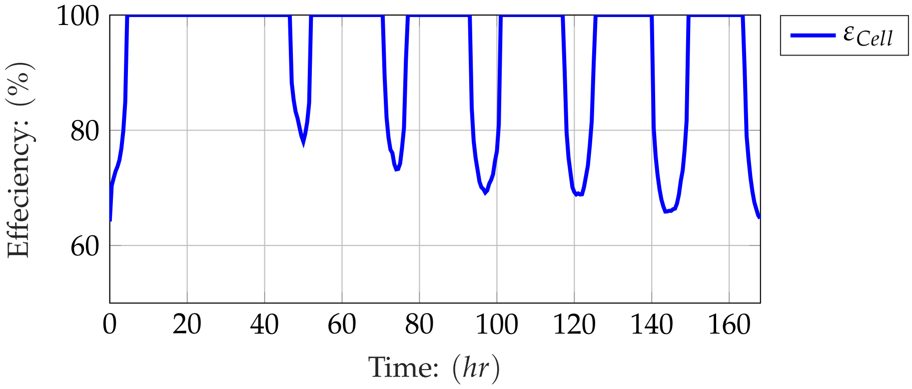

Figure 6.13: Dynamic response of the energy efficiency ε_{cell} when using excess solar power.

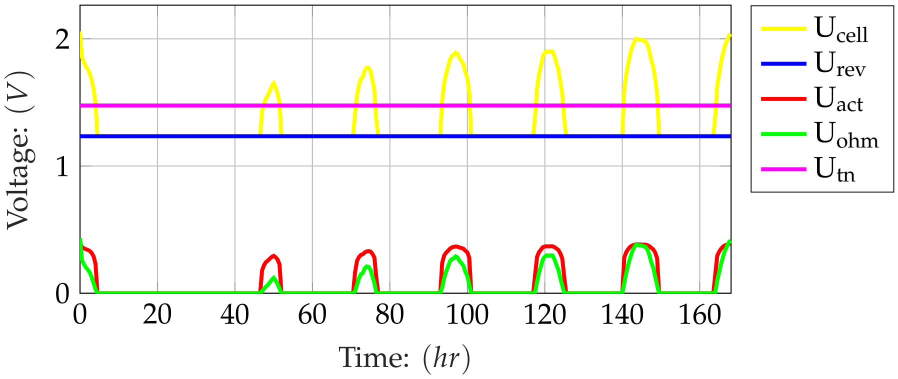

Figure 6.14: Dynamic response of cell potential U_{cell} and over potentials U_{act} and U_{ohm} when using excess solar power.

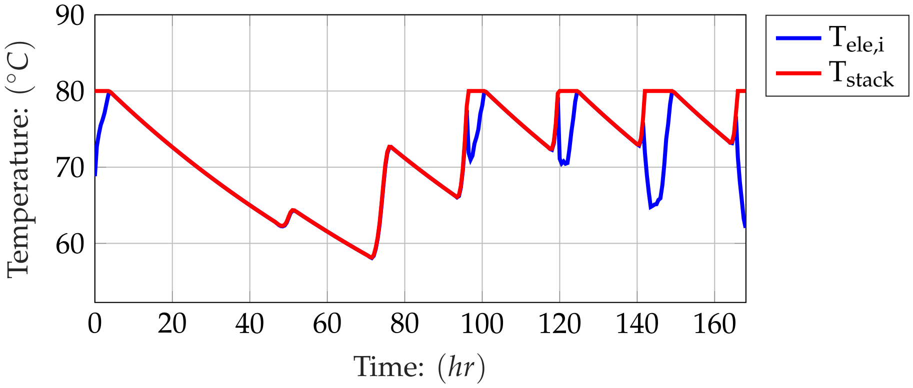

Figure 6.15: Dynamic response of stack temperature T_{stack} and temperature of electrolyte entering $T_{ele,i}$ when using excess solar power.

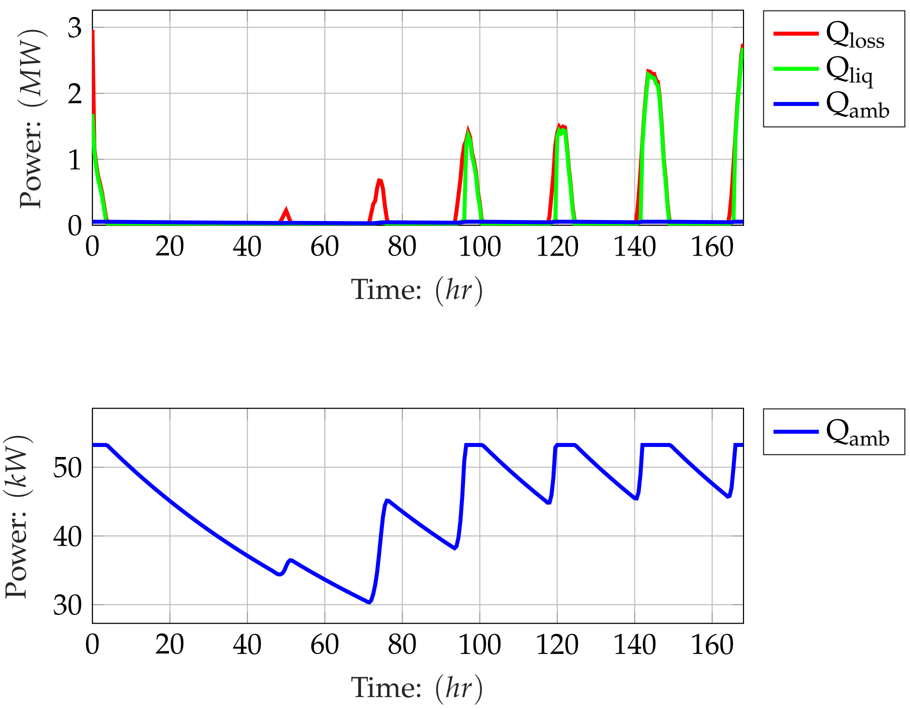

Figure 6.16: Dynamic response of heat flows Q_{loss}, Q_{liq} and Q_{amb} when using excess solar power.

Chapter 7

Dynamic Grid Frequency Regulation

Using the AWE system for excess power of IRES is not the only way of intergrading AWE in to the future landscape of more IRES. Dynamic regulation of the grid frequency might be another way that AWE could be utilised. The National Grid of Great Britain is a synchronous electrical grid and is phase-locked to $50Hz$. To achieve this the frequency need to be regulated by balancing the power production and power consumption as an excess of power will increase the grid frequency and a deficit will decrease it. In Figure 7.1 the frequency of the grid over a period of 24 hours is shown.

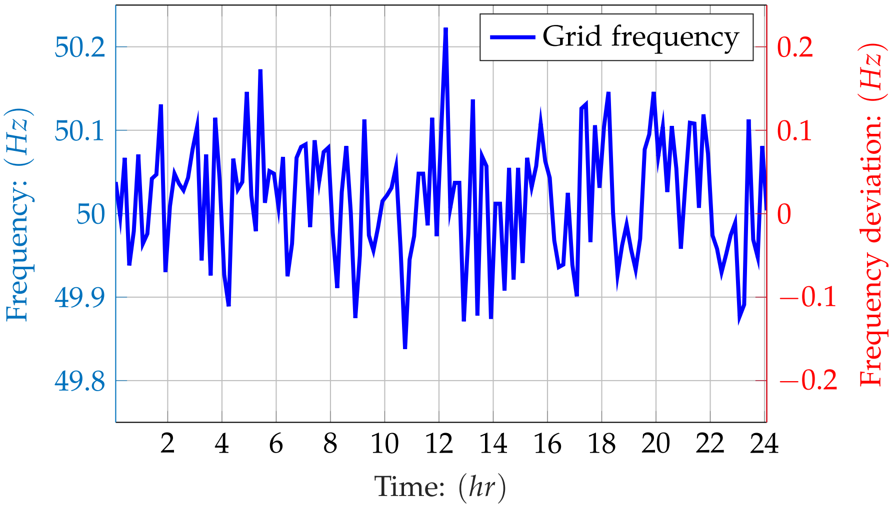

Figure 7.1: Frequency of the grid over a period of 24 hours in absolute frequency on the blue axis and deviation from $50Hz$ given on the red axis.

With dynamic regulation the load on the system will be based on the frequency deviations, consuming power when the frequency deviation is positive and producing power when it is negative. Because the AWE system can not produce power but only acts as a load the switch from positive to negative frequency deviation can just be shifted to a 50% load. This will still regulate the grid frequency when it falls below $50Hz$ as the deviation from the baseload of 50% will influence the supply and demand balance of power. In Figure 7.2 the method of converting frequency to a load percentage is shown. When the frequency falls $0.2Hz$ below $50Hz$ the AWE system is shut off and when the frequency exceeds $50Hz$ by $0.2Hz$ the AWE system will use 100% of its capacity. In the region of $\pm 0.015Hz$, the AWE system will operate at a 50% load.

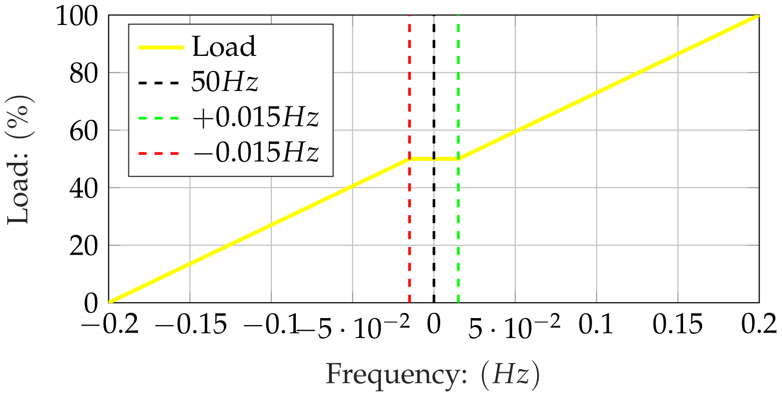

Figure 7.2: Load percentage based on frequency deviation from $50Hz$.

In Figure 7.3 the load found by converting the frequency from Figure 7.1 into power using the method shown in Figure 7.2 is presented. The baseload of 50% is added using a dotted line to show that the load is dominantly on the lower end of the baseload. This is partly due to the large spike in load around the 13 hour mark where the frequency deviation is exceeding $0.2Hz$.

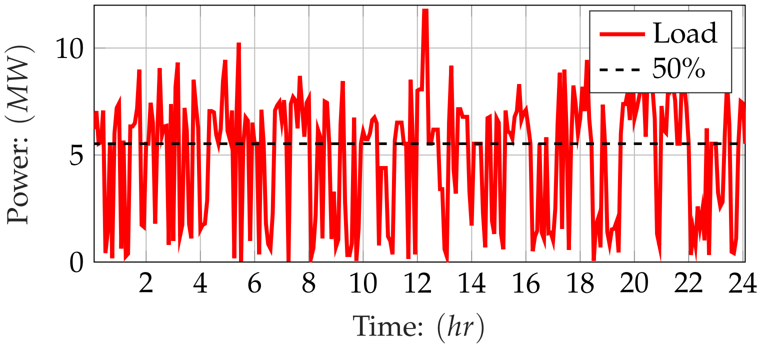

Figure 7.3: Load given in MW based on grid frequency.

The result from using the AWE system for frequency regulation is shown below. The current density, potentials, temperatures, heat flows and efficiency of the AWE stack is shown in the Figure 7.4, 7.5, 7.6, 7.7 and 7.8 respectively. In Figure 7.6 it can be seen that the temperature of the stack is held constant at 80°C as the system will almost always be subjected to a load when operating as a frequency regulator. This leads to a high mean efficiency of $\varepsilon_{cell} = 73.2\%$ because the system does not have time to cool down like it does when using excess power from IRES. Utilising power from IRES might therefore be more efficient for the AWE system through frequency regulation as opposed to just using excess power production.

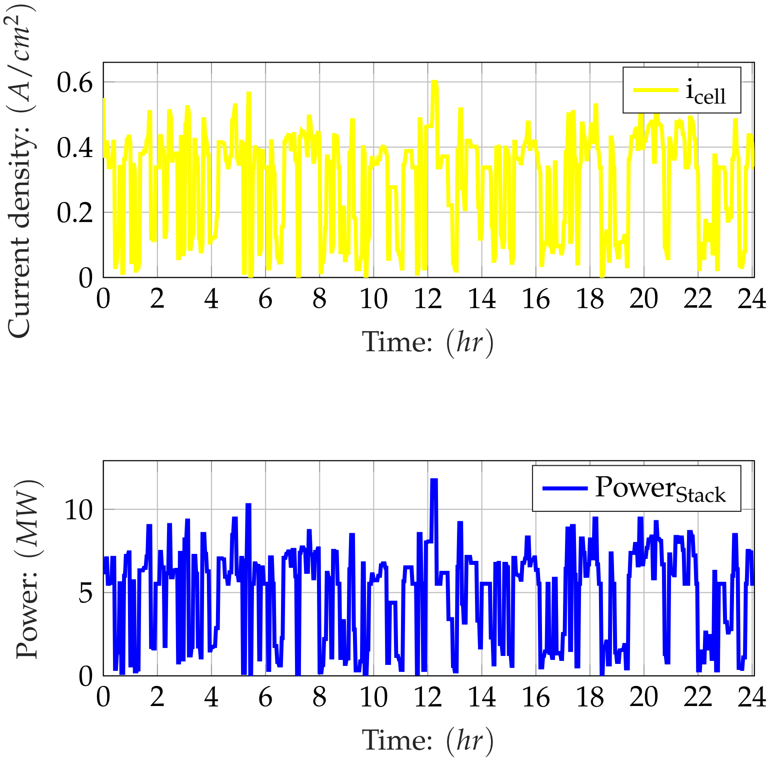

Figure 7.4: Power load and the corresponding current density using the AWE system for dynamic grid frequency regulation.

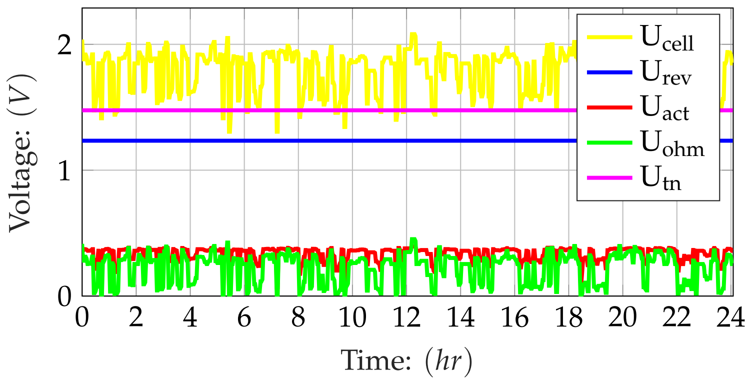

Figure 7.5: Dynamic response of cell potential U_{cell} and over potentials U_{act} and U_{ohm} under dynamic grid frequency regulation.

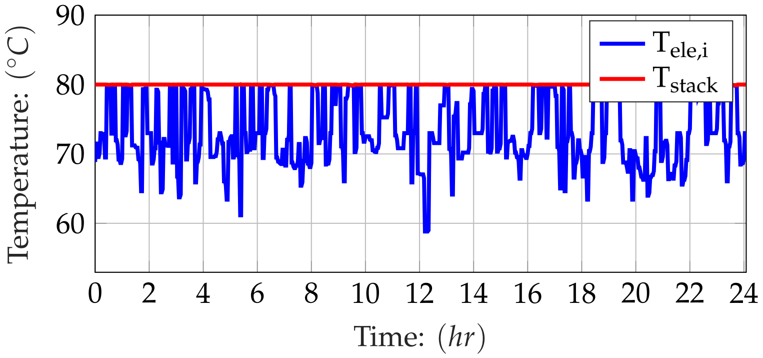

Figure 7.6: Dynamic response of stack temperature T_{stack} and temperature of electrolyte entering $T_{ele,i}$ under dynamic grid frequency regulation.

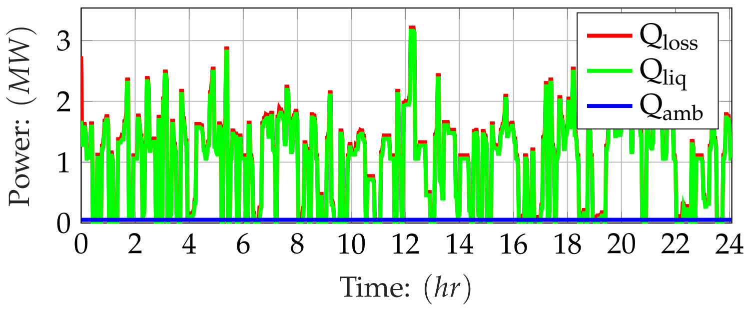

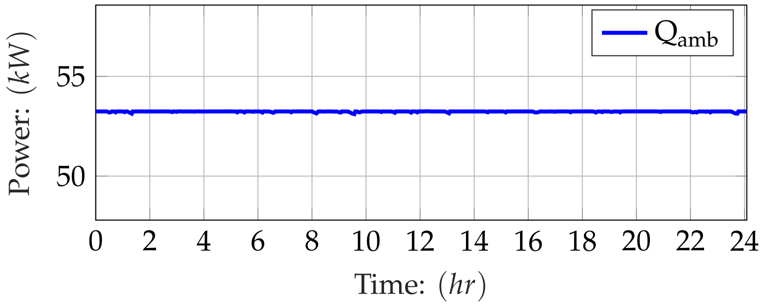

Figure 7.7: Dynamic response of heat flows Q_{loss}, Q_{liq} and Q_{amb} under dynamic grid frequency regulation.

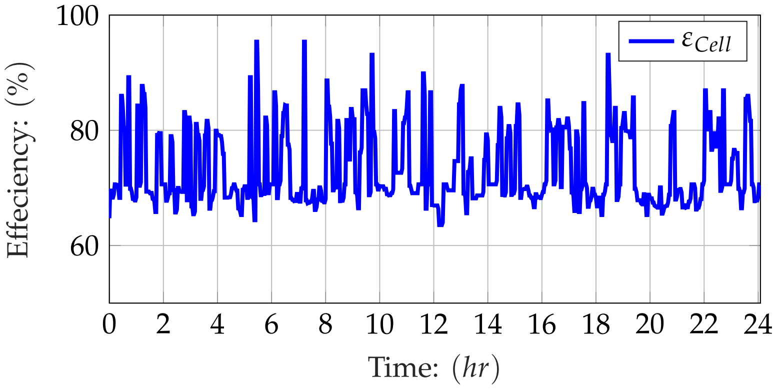

Figure 7.8: Dynamic response of the energy efficiency ε_{cell} under dynamic grid frequency regulation.

Chapter 8

Discussion

In the following chapter a discussion on parts of the model that did not present themselves through the results shown previously in chapter 5, 6 and 7. It was found that operating the AWE system as a dynamic frequency regulator had the benefit of keeping the system heated which would be beneficial to the efficiency of the AWE reaction. The mean efficiency over the period shown did however not show the dynamic frequency regulation operation to be more efficient. Looking only at temperature this should not be the case. The efficiency is however not only determined by temperature and current density does affect the efficiency more. This makes comparing the efficiencies of the different methods of operation more difficult and choosing the best method becomes a question of what is favoured efficiency or production of hydrogen.

One course of overpotentials that the model did not include is the overpotential associated with bubble build up on the electrodes [Haverkort and Rajaei 2021]. When current is supplied to the AWE cells and hydrogen and oxygen start forming the gas tends to stick to the surface of the electrodes as bubbles. This is of cause detrimental to the production of new hydrogen and oxygen as it can no longer form at the surface of the electrodes occupied by bubbles. another way bubble formation harms the process is the AWE reaction is that it lowers the conductivity between electrodes because the gasses act as an ionic insulator. The effect of the overpotential is however included in the activation overpotential U_{act}. This is because U_{act} was simply fitted to data from a real system that would be susceptible to losses due to bubbles. For the same reason, any other over potential not included in the model would be included in U_{act}. This does not invalidate the overall results of the report but it would mean that the exchange current densities fitted in chapter 3 are slightly lower than the actual values.

Chapter 9

Conclusion

In Chapter 2 the following problem statement was made.

How can an AWE system be modeled to predict the static and dynamic performance given a DC power input and how does the system perform under different modes of operation?

It was found that the static performance of the AWE process could be described by a sum of potentials describe by the operation conditions. The potential where the reversible potential U_{rev} and the two overpotentials associated with ohmic losses U_{ohm} and activation energy U_{act}. The reversible potential described as the potential needed to split water under reversible conditions was described using the Nernst equation making it dependent on temperature and pressure through thermodynamic activity. Furthermore, the thermodynamic activity was estimated using empirically-based equations found in [Sakas et al. 2022] to include the effect of the molarity of KOH in the electrolyte solution. The overpotential associated with ohmic losses U_{ohm} was found to be described by the specific conductivity and thickens between the electrodes, membrane and the two electrodes. For the specific conductivity of electrolyte empirically based equation was found relating it to temperature and molarity of KOH in the electrolyte solution. The specific conductivity of the zirfon membrane was provided by the manufacturer. For the electrodes, the specific conductivity was found to be negligible compared to the electrolyte and membrane and was therefore not included in the model. The activation overpotential was described by a single Butler–Volmer equation and was found to be dependent on temperature, current density and the exchange current densities of the OER and HER. The exchange current densities were later used as fitting parameters and an expression was found relating them to temperature. The static performance part of the model was fitted to data from an industrial-sized AWE system and the model was able to predict the performance with an r-squared value over $r^2 > 98\%$.

To include the dynamic performance of the AWE system energy and mass balances were made. The heat flows into and out of the AWE stack was found to be the heat generated by the losses of the AWE process Q_{loss}, the heat lost to the surroundings Q_{amb} and the sensible heat from cooled electrolyte reentering the stack Q_{liq}. The heat generated from the inefficiency of the AWE process was estimated using the thermal neutral potential U_{tn}, the cell potential U_{cell} and the current used by the AWE stack. The heat lost to the surroundings Q_{amb} was modelled analytically as the radiation and convection from a horizontal cylinder of the same surface area as AWE stack. The heat loss Q_{liq} was calculated simply as sensible heat between the cooled electrolyte entering the stack and the heat capacity of the stack. To balance the heat equations and control the temperature of the AWE stack the temperature of the electrolyte reentering the system was controlled by a heat exchanger. The heat exchanger was modelled as a counter-flow heat exchanger using the NTU method as all inlet and outlet temperature was not known. The mass flow of cooling water is then controlled with a P controller to reach the desired operating temperature of the AWE stack. Under synthetic load, the model was able to predict the behaviour of Q_{loss}, Q_{liq} and Q_{amb} at different temperatures and current densities. Q_{liq} was shown to follow the dynamics of Q_{loss} when the stack was at the desired operational temperature to balance the heat equations.

Finally, the model developed was tested under different modes of operation. First, a series of synthetic tests were made to assess the performance of the AWE during a step in current, the heating process and the cool down process. Here it was found that the heating process was orders of magnitude faster than the cool down process. The model was also tested using excess power from IRES yielding high mean energy efficiencies of $\varepsilon_{cell} = 73.9\%$ using wind power and $\varepsilon_{cell} = 75.1\%$ using solar power. Finally, the model was used for dynamic frequency regulation and it was found that in this mode of operation the AWE stack temperature was held constant at the desired operational temperature yielding a similarly high mean energy efficiency of $\varepsilon_{cell} = 73.2\%$.

Bibliography

Demitri, Bessarabov et al. (2016). *PEM Electrolysis for Hydrogen Production Principles and Applications*. Taylor & Francis Gruop.

European Union, Council of the (2021). *Fit for 55 package proposals (CBAM, ETD and SCF) - Progress report*. URL: `https://data.consilium.europa.eu/doc/document/ST-14574-2021-INIT/en/pdf` (visited on 05/27/2022).

Gaskell, D.R. (2001). "Thermodynamic Activity". In: *Encyclopedia of Materials: Science and Technology*. Ed. by K.H. Jürgen Buschow et al. Oxford: Elsevier, pp. 9164–9169. ISBN: 978-0-08-043152-9. DOI: `https://doi.org/10.1016/B0-08-043152-6/01653-3`. URL: `https://www.sciencedirect.com/science/article/pii/B0080431526016533`.

Gilliam, R.J. et al. (2007). "A review of specific conductivities of potassium hydroxide solutions for various concentrations and temperatures". In: *International Journal of Hydrogen Energy* 32.3. Fuel Cells, pp. 359–364. ISSN: 0360-3199. DOI: `https://doi.org/10.1016/j.ijhydene.2006.10.062`. URL: `https://www.sciencedirect.com/science/article/pii/S0360319906005428`.

Godula-Jopek, Agata (2015). *Hydrogen production: by electrolysis*. John Wiley & Sons.

government, The danish (2021). *Køreplan for et grønt Danmark*. URL: `https://www.regeringen.dk/aktuelt/publikationer-og-aftaletekster/koereplan-for-et-groent-danmark/` (visited on 05/27/2022).

Haverkort, J.W. and H. Rajaei (2021). "Voltage losses in zero-gap alkaline water electrolysis". In: *Journal of Power Sources* 497, p. 229864. ISSN: 0378-7753. DOI: `https://doi.org/10.1016/j.jpowsour.2021.229864`. URL: `https://www.sciencedirect.com/science/article/pii/S037877532100402X`.

Jiang, Tao (May 2020). "Development of Alkaline Electrolyzer Electrodes and Their Characterization in Overall Water Splitting". Theses. Université Bourgogne Franche-Comté. URL: `https://tel.archives-ouvertes.fr/tel-03270903`.

Kojima, H. et al. (2018). "Development of dynamic simulator of alkaline water electrolyzer for optimizing renewable energy systems". In: *Journal of International Council on Electrical Engineering* 8.1, pp. 19–24. DOI: `10.1080/22348972.2018.1436931`. eprint: `https://doi.org/10.1080/22348972.2018.1436931`. URL: `https://doi.org/10.1080/22348972.2018.1436931`.

Laliberté, Marc (2009). “A Model for Calculating the Heat Capacity of Aqueous Solutions, with Updated Density and Viscosity Data”. In: *Journal of Chemical & Engineering Data* 54.6, pp. 1725–1760. ISSN: 0021-9568. DOI: `10.1021/je8008123`. URL: `https://doi.org/10.1021/je8008123`.

Lamy, Claude and Pierre Millet (2020). “A critical review on the definitions used to calculate the energy efficiency coefficients of water electrolysis cells working under near ambient temperature conditions”. In: *Journal of Power Sources* 447, p. 227350. ISSN: 0378-7753. DOI: `https://doi.org/10.1016/j.jpowsour.2019.227350`. URL: `https://www.sciencedirect.com/science/article/pii/S0378775319313436`.

Lupi, C., A. Dell’Era, and M. Pasquali (2009). “Nickel–cobalt electrodeposited alloys for hydrogen evolution in alkaline media”. In: *International Journal of Hydrogen Energy* 34.5, pp. 2101–2106. ISSN: 0360-3199. DOI: `https://doi.org/10.1016/j.ijhydene.2009.01.015`. URL: `https://www.sciencedirect.com/science/article/pii/S0360319909000524`.

Minke, Christine et al. (May 2021). “Is iridium demand a potential bottleneck in the realization of large-scale PEM water electrolysis?” In: *International Journal of Hydrogen Energy* 46. DOI: `10.1016/j.ijhydene.2021.04.174`.

NASA Glenn Coefficients for CalculatingThermodynamic Properties ofIndividual Species (Sept. 2002). Tech. rep. 20020085330. NASA Glenn Research Center Cleveland, OH United States.

"Peter Styring" "Elsje Alessandra Quadrelli", "Katy Armstrong" (2015). *Carbon Dioxide Utilisation Closing the Carbon Cycle*. Elsevier.

Rodríguez, Jesús et al. (2019). “Simple and Precise Approach for Determination of Ohmic Contribution of Diaphragms in Alkaline Water Electrolysis”. In: *Membranes* 9.10. ISSN: 2077-0375. DOI: `10.3390/membranes9100129`. URL: `https://www.mdpi.com/2077-0375/9/10/129`.

Sakas, Georgios et al. (2022). “Dynamic energy and mass balance model for an industrial alkaline water electrolyzer plant process”. In: *International Journal of Hydrogen Energy* 47.7, pp. 4328–4345. ISSN: 0360-3199. DOI: `https://doi.org/10.1016/j.ijhydene.2021.11.126`. URL: `https://www.sciencedirect.com/science/article/pii/S0360319921045110`.

Schroeder, Daniel V. (2000 - 2000). *An introduction to thermal physics*. eng. San Francisco, CA.

Shen, Xiaojun et al. (2018). “Experimental study on the external electrical thermal and dynamic power characteristics of alkaline water electrolyzer”. In: *International Journal of Energy Research* 42.10, pp. 3244–3257. DOI: `https://doi.org/10.1002/er.4076`. eprint: `https://onlinelibrary.wiley.com/doi/pdf/10.1002/er.4076`. URL: `https://onlinelibrary.wiley.com/doi/abs/10.1002/er.4076`.

Soltani, Reza, Marc Rosen, and Ibrahim Dincer (Oct. 2014). “Assessment of CO2 capture options from various points in steam methane reforming for hydrogen production". In: *International Journal of Hydrogen Energy* 39. DOI: `10.1016/j.ijhydene.2014.09.161`.

Spiegel, Colleen (2008). "Chapter 6 - Heat Transfer". In: *PEM Fuel Cell Modeling and Simulation Using Matlab*. Ed. by Colleen Spiegel. Burlington: Academic Press, pp. 127–166. ISBN: 978-0-12-374259-9. DOI: `https://doi.org/10.1016/B978-012374259-9.50007-0`. URL: `https://www.sciencedirect.com/science/article/pii/B9780123742599500070`.